
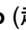



# Numerical investigations of three-dimensional flows around a cylinder attaching with symmetric strips

Cite as: Phys. Fluids **33**, 075101 (2021); <https://doi.org/10.1063/5.0055280>

Submitted: 27 April 2021 . Accepted: 08 June 2021 . Published Online: 01 July 2021

 Chunhui Ma (马春卉),  Weiwen Zhao (赵伟文), and  Decheng Wan (万德成)



View Online



Export Citation



CrossMark

Physics of Fluids

SPECIAL TOPIC: Flow and Acoustics of Unmanned Vehicles

Submit Today!



# Numerical investigations of three-dimensional flows around a cylinder attaching with symmetric strips

Cite as: Phys. Fluids **33**, 075101 (2021); doi: 10.1063/5.0055280

Submitted: 27 April 2021 · Accepted: 8 June 2021 ·

Published Online: 1 July 2021





View Online



Export Citation



CrossMark

Chunhui Ma (马春卉),<sup>1</sup>  Weiwen Zhao (赵伟文),<sup>1</sup> and Decheng Wan (万德成)<sup>1,2,a)</sup> 

## AFFILIATIONS

<sup>1</sup>Computational Marine Hydrodynamics Lab (CMHL), School of Naval Architecture, Ocean and Civil Engineering, Shanghai Jiao Tong University, Shanghai 200240, China

<sup>2</sup>Ocean College, Zhejiang University, Zhoushan 316021, China

<sup>a)</sup>Author to whom correspondence should be addressed: [dcwan@sjtu.edu.cn](mailto:dcwan@sjtu.edu.cn)

## ABSTRACT

Minor changes to the surface of a cylinder can significantly influence the associated flow characteristics. This paper describes a three-dimensional numerical investigation of a cylinder attached with symmetric strips in a uniform flow at  $Re = 3900$ . The location ( $20^\circ \leq \alpha \leq 130^\circ$ ), thickness ( $0.01D \leq t \leq 0.08D$ ), and coverage ( $5^\circ \leq \beta \leq 100^\circ$ ) of the strips are selected for study. Two flow modes, patterns A and D, can be characterized in the flow around this passive turbulence control cylinder by their vortex enhancement and suppression effects. The Strouhal number of pattern A is very close to the response of a smooth cylinder. For cylinders with the upper strip located at  $\alpha \leq 90^\circ$  from the front stagnation point, the lift force correlation in the spanwise direction is enhanced by the forced flow separation. When the front edge of the upper strip is fixed at  $\alpha = 60^\circ$ , the thickness of the strips plays a vital role: the drag and lift force increase linearly as the thickness increases, whereas the Strouhal number and the vortex shedding frequency decrease.

Published under an exclusive license by AIP Publishing. <https://doi.org/10.1063/5.0055280>

## I. INTRODUCTION

The flows around a cylinder can be widely found in nature and engineering. Although the geometric shape is simple, this classic case potentially contains three fundamental ingredients of complicated flow phenomena—a boundary layer, a free shear layer, and a wake—which have fascinated scholars for centuries.

One of the main parameters determining the characteristics of flows past a cylinder is the Reynolds number  $Re = \frac{DU_\infty}{\nu}$ , where  $D$  represents the relative length (the diameter for a cylinder),  $U_\infty$  is the velocity of the incoming flow, and  $\nu$  represents the kinematic viscosity coefficient. With increasing Reynolds number, the flow undergoes tremendous changes. The wake becomes unstable and eventually triggers vortex shedding on alternate sides of the cylinder beyond a critical Reynolds number  $Re \approx 47$ .<sup>1,2</sup> Observations show that the vortices do not vary along the cylinder's spanwise direction for  $40 < Re < 200$ , indicating a two-dimensional flow.<sup>3</sup> With further increases in  $Re$ , the vortex shedding forms cells and the flow becomes three-dimensional.<sup>4</sup> Very fine time steps and mesh resolutions should be used to simulate Reynolds numbers larger than 190 in a sufficient three-dimensional domain to obtain reliable numerical simulations,<sup>5</sup> not to mention the

cases at various subcritical Reynolds numbers. For example, the flow around a cylinder at  $Re = 3900$  has been extensively studied by numerical simulations. Two-dimensional simulations using the Reynolds-averaged Navier–Stokes (RANS) method at  $Re = 3900$  may involve a relatively large drag coefficient, where the basic suction coefficient is more than twice that observed experimentally.<sup>6</sup> Three-dimensional numerical simulations using the large-eddy simulation (LES), hybrid RANS/LES, and detached-eddy simulation (DES) can capture the details of the flow field and obtain results consistent with experimental data.<sup>7–10</sup> Furthermore, Ji *et al.*<sup>11</sup> used an iterative immersion boundary method combined with a simple wall-layer to simulate the turbulent flow around a three-dimensional stationary cylinder at  $Re = 3900$  and obtained excellent mean flow and turbulence statistics. The length-to-diameter ratio of the cylinder should be at least  $\pi$  in three-dimensional numerical studies of the flow around a cylinder to allow the vortex to develop fully in the span direction. It is well known that vortex shedding causes pressure fluctuations on the cylinder surface,<sup>12,13</sup> which induce periodic fluctuations in the lift force. The nondimensional shedding frequency—the Strouhal number  $St = \frac{Df_s}{U_\infty}$ , where  $f_s$  is the vortex-shedding frequency—is another important parameter in describing the

flow around bluff bodies.  $St$  is closely related to the fluctuating lift and remains practically constant at 0.2 throughout the subcritical Reynolds number range  $300 \leq Re \leq 3 \times 10^5$ .<sup>14</sup>

In nature, some circular cylindrical structures are exposed to the outside environment for a long time, such as risers immersed in seawater. The salt crystals that form on the riser surfaces change the original fluid–structure interaction characteristics, causing fatal damage to the structures. Therefore, the study of small changes in the surface of a circular cylinder has attracted considerable attention. For example, research on the surface roughness shows that the transition to turbulent flow occurs much earlier on the surface of a rough cylinder than on a smooth cylinder.<sup>15,16</sup> The study of the effect of tripping-wire positions on the flow around a circular cylinder shows that the Strouhal number distinguishes four flow patterns in the range  $1.3 \times 10^3 < Re < 9.6 \times 10^4$ .<sup>17</sup> In pattern A, the nearly smooth cylinder has  $St \approx 0.2$ ; the Strouhal number is greater than 0.2 in patterns B and C because the tripping wires promote the development of a turbulent boundary layer. Finally, pattern D represents the forced separation of the flow, where the Strouhal number is less than 0.2. These four flow patterns are related to the boundary layer transition and flow separation. Hover *et al.*<sup>18</sup> studied the impact on the flow of symmetric tripping wires located at  $\pm 70^\circ$  from the front stagnation point in the subcritical Reynolds number range. They observed that pattern D is not excited when the height of the wire is  $0.003D$ . Moreover, Hover *et al.* tested whether the wire position under flow pattern B could slightly suppress vibration when the cylinder was free to move. The near-wake instability and shear-layer separation of the effects of parallel wires were explored using high-image-density particle image velocimetry.<sup>19</sup> Bhattacharya and Gregory<sup>20</sup> studied the three-dimensional effect of cylindrical wake by symmetrically arranging segmented plasma actuators on the cylindrical surface. They found that the shedding vortices were severely weakened near the wake and stretched along the spanwise with high power. Feng *et al.*<sup>21</sup> found that jet control to the cylinder can change the wake three-dimensional pattern.

Besides, for the convenience and feasibility of research and practical applications, some scholars have carried out research on the effects of adding rough and smooth strips to the cylinder surface.<sup>16,22,23</sup> Bernitsas and his team used sandpaper strips to alter the surface of a circular cylinder in an attempt to control flow-induced vibration (FIV), a method known as passive turbulence control (PTC).<sup>22</sup> Their purpose was to excite vibration to obtain greater energy and to study whether the height of the surface strips is more significant than the surface roughness.<sup>24–26</sup> In line with Nakamura's research, a successful high-Reynolds number phenomenon was obtained by a smooth cylinder with rough strips attached and not by the distributed roughness. Then, thick strips have also been attached to the cylindrical surface to excite vibration and energy harvesting.<sup>27</sup> Moreover, some scholars have performed multi-cylinder experimental research to study more vibration mechanisms, such as vortex-induced vibration (VIV) and galloping.<sup>28,29</sup> Numerical simulations have also contributed to the study of the FIV response of a cylinder with strips using a 2D RANS method.<sup>30–32</sup> However, because the geometric model is free to vibrate perpendicular to the incoming flow, this research about strips effecting has mainly focused on the structural vibration response, such as the amplitude and frequency of the cylinder. Previous studies have seldom focused on the pressure distribution, flow separation point, and the correlation of the span direction around the cylinder under the

influence of strips although these hydrodynamic mechanisms are indispensable for studying the flow around the structure.

These gaps in existing research motivated the present study. We use the three-dimensional numerical simulations to study the flow around a stationary cylinder with symmetric strips attached in a uniform flow at  $Re = 3900$ . There are two reasons for choosing this Reynolds number. First, the flow around the cylinder at  $Re = 3900$  is representative because of  $St \approx 0.2$  in the subcritical Reynolds number range. Second, this is a reliable case for comparison as it has been discussed in detail in a number of previous studies, including circular and other shape cross section.<sup>33,34</sup> On this basis, the advantage that the strip parameters (i.e., position, coverage, thickness) can be independently adjusted is used to analyze the hydrodynamic characteristics of the cylinder. This aims of this study are as follows:

- 1) Compared with a smooth cylinder, we attempt to determine how the position of the strips enhances or inhibits the formation of vortices.
- 2) We identify whether the existence of strips is beneficial to increasing the correlation of the force in the cylinder span direction, a question that is crucial in making the cylinder longer or even flexible.
- 3) We study how the thickness or coverage of the strips at a fixed location affects the flow.
- 4) Finally, this study provides a reference for subsequent research on the strip parameters for vibrating cylinders.

There are two points to be noted in advance. First, the strips in the following numerical simulations are effectively smooth surfaces, regardless of roughness. This is because, in experiments, the roughness of the strips has little effect on the flow compared with the thickness of the strips. The abbreviation PTC, for passive turbulence control, indicates that the strips are intended to control the occurrence of turbulence passively.<sup>35</sup> The various PTC cylinders with different parameters are referred to as  $Ph - \alpha - \beta$ , where  $h$  refers to the ratio percentage of the thickness  $t$  of the strip to the diameter of the cylinder, such as  $h = 5$  indicates that the thickness of the strip is 5% of the diameter;  $\alpha$  refers to the angle from the upper strip's upstream edge to the stagnation point in front of the cylinder; and  $\beta$  is the coverage area. For example, P5-60-5 refers to a PTC cylinder with parameter values of  $h = 5$ ,  $\alpha = 60^\circ$ ,  $\beta = 5^\circ$ .

The structure of this article is as follows. Section II describes the numerical models and methods used. The flow around a smooth cylinder at  $Re = 3900$  is examined in Sec. III to verify the reliability of the numerical method and the solver. Section IV presents numerical simulation results for  $20^\circ \leq \alpha \leq 130^\circ$  with  $\beta = 20^\circ$  and  $h = 5$ . On this basis, the location is fixed as  $\alpha = 60^\circ$ , and the influence of the strip coverage ( $5^\circ \leq \beta \leq 100^\circ$ ) and thickness ( $0.01D \leq t \leq 0.05D$ ) on the hydrodynamics of the cylinder is examined in Sec. V. Finally, the results of this study are summarized in Sec. VI.

## II. NUMERICAL METHOD AND COMPUTATIONAL DETAILS

The three-dimensional numerical simulations in this study were performed using a six-degrees-of-freedom (6DoF) computational fluid dynamics (CFD) solver, naoe-FOAM-SJTU,<sup>36</sup> which was developed on the open-source toolbox OpenFOAM. The solver has been verified by many hydrodynamic and ocean engineering problems and is

constantly being supplemented and improved to expand its applicability to more problems.<sup>37–42</sup> The PIMPLE algorithm (combined PISO-SIMPLE) was adopted to solve the coupling of pressure and velocity.<sup>43</sup> PIMPLE treats each time step as a steady-state and executes the SIMPLE corrector outside the PISO loop. It can run stably on larger time steps with a Courant–Friedrichs–Lewy number greater than one. In this section, the governing equations and turbulence model are first discussed, and then the computational details are provided.

**A. Numerical method**

In this study, the  $k-\omega$  shear stress transport based on delayed DES (SST-DDES) was used to resolve the large-separation flow under a high Reynolds number. SST-DDES is a hybrid RANS-LES method that is similar to the SST  $k-\omega$  RANS model in the near-wall attachment boundary region and similar to the LES sub-grid model in the separated free shear flow region. Moreover, by introducing a delay function to prevent the RANS calculation area from switching to LES mode prematurely, the grid-induced separation problems caused by modeled stress depletion can be overcome. For an incompressible viscous flow, the continuity equation and the turbulence momentum equation are given by

$$\nabla \cdot \mathbf{U} = 0, \tag{1}$$

$$\frac{\partial \mathbf{U}}{\partial t} + \nabla \cdot (\mathbf{U} - \mathbf{U}_g)\mathbf{U} - \nabla \cdot (\nu_{eff} \nabla \mathbf{U}) - (\nabla \mathbf{U}) \cdot \nabla \nu_{eff} = -\frac{1}{\rho} \nabla p. \tag{2}$$

Here,  $\mathbf{U}$ ,  $p$ , and  $\rho$  represent the velocity, pressure, and density of incompressible fluid,  $\mathbf{U}_g$  represents the grid velocity, and  $\nu_{eff}$  is the effective viscosity composed of molecular viscosity  $\nu$  and turbulent eddy viscosity  $\nu_t$ .

The SST transport equations are given by

$$\frac{\partial k}{\partial t} + \nabla \cdot (\mathbf{U} - \mathbf{U}_g)k = \tilde{G} - \frac{k^{3/2}}{l} + \nabla \cdot [(\nu + \alpha_k \nu_t) \nabla k], \tag{3}$$

$$\begin{aligned} \frac{\partial \omega}{\partial t} + \nabla \cdot (\mathbf{U} - \mathbf{U}_g)\omega &= \gamma S^2 - \beta \omega^2 + \nabla \cdot [(\nu + \alpha_\omega \nu_t) \nabla \omega] \\ &+ (1 - F_1) CD_{k\omega}. \end{aligned} \tag{4}$$

Here,  $\tilde{G} = \min(\nu_t S^2, c_1 \beta^* k \omega)$ , depending on turbulent eddy viscosity  $\nu_t$ , invariant measure of the strain rate  $S$ ; turbulent kinetic energy  $k$  and dissipation rate  $\omega$ ; and  $l$  is the turbulence length;  $F_1$ ,  $\beta$ ,  $\gamma$ ,  $\alpha_\omega$ , and  $\alpha_k$  are constants; for the values, refer to Zhao and Wan.<sup>6</sup>

**B. Computational details**

Based on the 6DoF CFD solver, the flow around a cylinder of diameter  $D = 0.0381$  m and length  $L = \pi D$  was studied both with and without strips. The number of degrees of freedom was set to zero in the solver because the cylinder considered in this study was assumed to be stationary. The cylinder was located in a uniform flow of speed  $U_\infty = 0.1023$  m/s along the  $x$ -direction. The geometric model is shown in Fig. 1(a). A  $20D \times 30D \times \pi D$  cuboid was selected for the fluid domain, and the cylinder’s gravity center was located at  $10D$  from the distance to the inlet boundary condition along the longitudinal centerline of the domain;  $y$  is vertical to the direction of incoming flow velocity, and  $z$  is the direction of the cylinder span. At the inlet boundary, the velocity was set to  $U_\infty$ , and a zero pressure gradient was prescribed. The surface of the cylinder adopted the non-slip boundary condition. The front, back, top, and bottom lateral boundary conditions were set to be symmetry plane in the solver. At the outlet boundary, the velocity was specified as having a zero gradient and the pressure was set to zero. Figure 1(b) illustrates a PTC cylinder with two slender strips attached symmetrically on both sides. The symbol  $\alpha$  refers to the angle between the front edge of the upper strip and the flow stagnation point in front of the cylinder,  $\beta$  is the coverage, and  $t$  is the thickness of the strip.

Figure 2 shows global and close-up views of the structured grid of the numerical model. The boundary layer around the cylinder is more refined and more grid cells are allocated to downstream nodes. The grids of the smooth cylinder comprised 1 242 240 cells with the circumferential 252 nodes, the radial 121 nodes, and spanwise 30 nodes. The minimum radial cell thickness  $\Delta r/D$  from the cylindrical surface is 0.001. The dimensionless wall spacing of the first layer close to the wall grid satisfies  $y^+ \approx 1$ , ensuring that the first layer unit is located in the viscous sub-layer. Note that, because this study involves multiple examples with various strip parameters, the possible positions of the strips are divided into blocks when the smooth

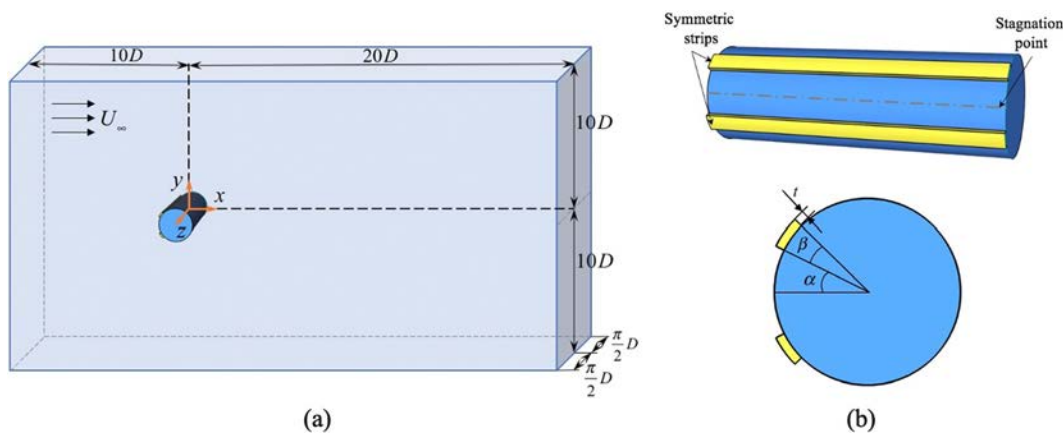


FIG. 1. Computational domain and geometric model. (a) Computational domain for flow around a cylinder, (b) geometric model of PTC cylinder.

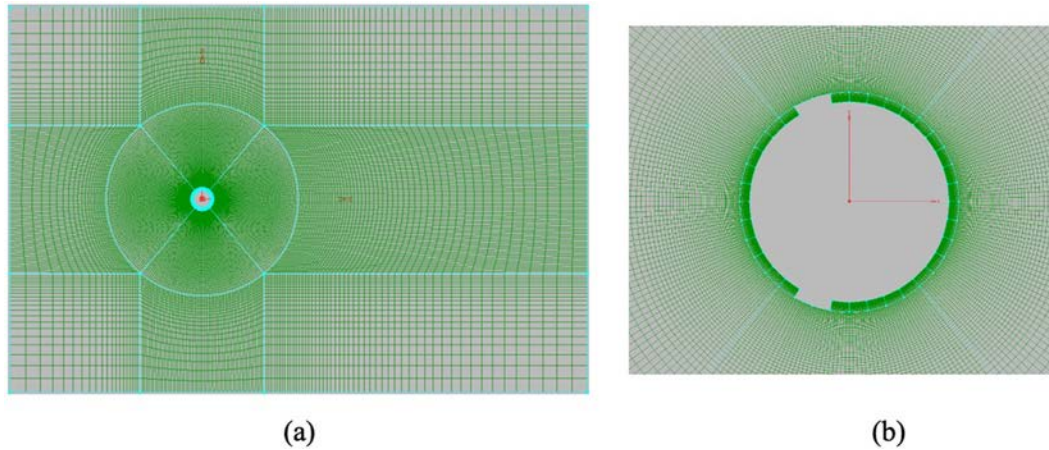


FIG. 2. Computational mesh. (a) Global view, (b) close-up view.

cylindrical grid is drawn to avoid errors caused by the replacement of the grid [Fig. 2(b)]. This ensures that changing the strips does not affect the other parts of the cylinder, and so the results from each calculation case can be reliably compared.

### III. VALIDATION: FLOW AROUND A SMOOTH CYLINDER

The flow past a smooth cylinder at  $Re = 3900$  has been validated in previous experimental and numerical studies.<sup>7,34,44,45</sup> To provide a brief validation that verifies the reliability of the solver and as a standard calculation example for PTC cylinder comparison, this section compares the results obtained for a smooth cylinder with previous work.

The flow parameters obtained by the present numerical method and those from previous experiments<sup>34,44,46</sup> and numerical simulations<sup>45,47</sup> are summarized in Table I, including the drag force coefficient  $\overline{C}_d$ , Strouhal number  $St$ , base suction coefficient  $C_{p_b}$ , separation angle  $\phi_s$ , length of the mean recirculation region  $L_{rec}/D$ , and minimum flow velocity  $\overline{U}_{min}$ . The parameters obtained by the present simulation scheme are within the range of the experimental data and previous numerical simulation results. Note that the data in the table largely depend on the average calculation time of the cases.<sup>7,44,48</sup> As the average calculation time increases, the circulation region becomes substantially longer and the basic suction coefficient and average drag coefficient decrease.<sup>7</sup> Thus, the basic suction coefficient in the present study is slightly smaller than the other values, perhaps due to the longer average calculation time,  $T^* = TU_\infty/D \approx 268.5$ , where  $T$  is the simulation time. We set  $T^* \approx 268.5$  in all PTC cylinders to eliminate

the error caused by the average calculation time. The minimum flow velocity  $\overline{U}_{min}$  in the recirculation zone obtained by the numerical simulations is greater than the experimental values. This may be due to an earlier transition in the separated shear layer as the result of some external disturbances.<sup>45</sup>

Next, the distributions of local pressure and skin friction around the center cross section of the cylinder were examined with respect to the peripheral angle  $\phi$ . The dimensionless parameter  $C_p$  can be used to represent the local static pressure distribution,

$$C_p = \frac{p - p_\infty}{\frac{1}{2}\rho U_\infty^2}. \tag{5}$$

Here,  $p = p(\phi)$  represents the pressure at the cylinder's peripheral angle  $\phi$  and  $p_\infty$  represents the static pressure of the flow at infinity. It can be seen from Fig. 3 that the distribution of local pressure (blue line) is in good agreement with experimental results.<sup>49</sup>

The cylinder skin friction can be represented in terms of the cylinder surface shear stresses and Reynolds number as<sup>50</sup>

$$\tau = \frac{\tau_0}{\rho U^2} \sqrt{Re}. \tag{6}$$

The boundary layer separates lamarily at  $\phi_s = 85.7^\circ$  ( $\phi_s = 274.3^\circ$ ), as can be seen from the red line in Fig. 3. Boundary separation occurs when the skin friction vanishes. If  $\tau = 0$ , the velocity gradient on the cylindrical surface is equal to zero, which is the flow boundary layer separation condition. The present  $Re$  was studied beyond wake transition regimes, and the  $\phi_s - Re$  relationship is monotonic, in line with the following equation:<sup>4</sup>

TABLE I. Flow parameters from smooth cylinder flow,  $Re = 3900$ .

Data source	$\overline{C}_d$	$St$	$-C_{p_b}$	$\phi_s$	$L_{rec}/D$	$\overline{U}_{min}$
Experiment <sup>34,44,46</sup>	$0.99 \pm 0.05$	$0.215 \pm 0.005$	$0.88 \pm 0.05$	$86.0^\circ \pm 2$	$1.4 \pm 0.1$	$0.24 \pm 0.1$
DNS <sup>47</sup>	1.03	0.215	0.87	$86.5^\circ$	1.2	...
LES <sup>45</sup>	1.00	0.210	0.93	$88.0^\circ$	1.35	0.37
Present	1.003	0.212	0.863	$85.7^\circ$	1.405	0.342

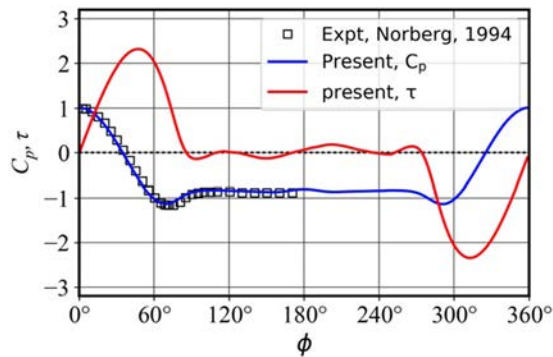


FIG. 3. Pressure and skin friction distribution of smooth cylinder.

$$\phi_s = 78.8 + 505Re^{-1/2} (270 \leq Re \leq 10^5). \quad (7)$$

The distribution of streamwise and normal velocity at three locations downstream of the smooth cylinder is plotted in Fig. 4. The streamwise velocity close to the cylinder is U-shaped, and that downstream is V-shaped. The normal velocity exhibits an antisymmetric distribution profile. The results of the present simulations are consistent with the experimental data (represented by an open circle in Fig. 4).<sup>34</sup> Therefore, the numerical method is reliable and accurate for simulating the flow past a smooth cylinder at  $Re = 3900$  using the naoe-FOAM-SJTU solver. The results in this section provide a comparison with the PTC cylinders under the same Reynolds number.

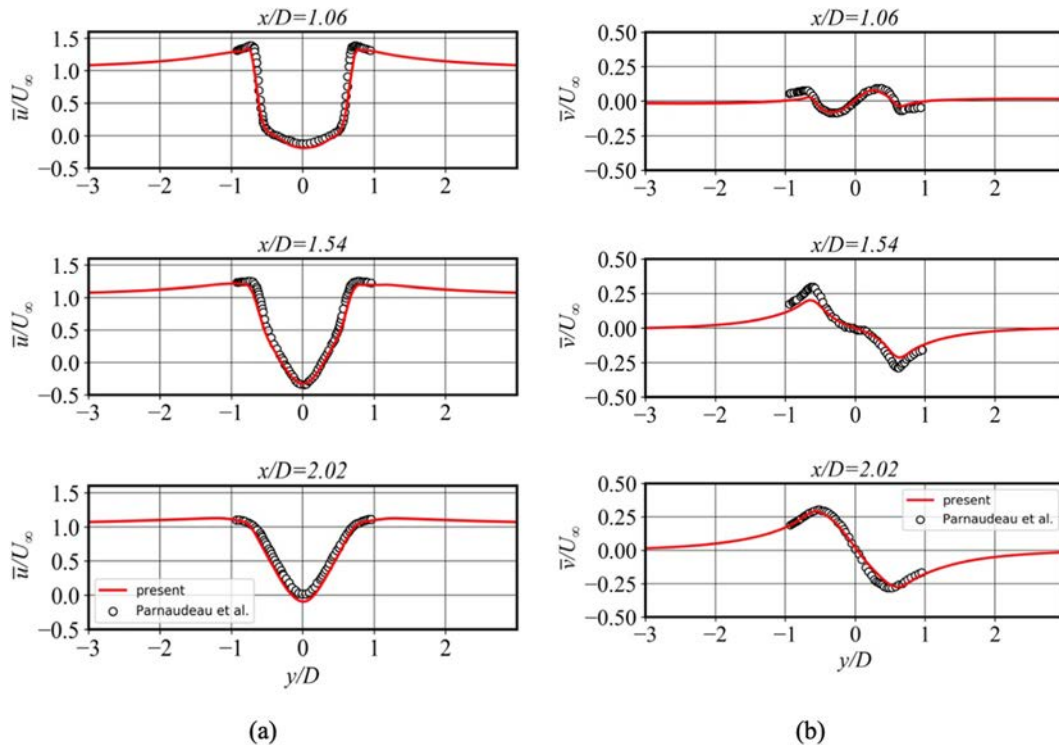


FIG. 4. Mean velocity at three locations downstream of the smooth cylinder. (a) Streamwise velocity, (b) normal velocity.

#### IV. EFFECTS OF STRIPS AT DIFFERENT LOCATIONS

This section presents and discusses the details obtained from the flow past a stationary PTC cylinder at  $Re = 3900$  with different strip locations. We consider the case of two symmetric and parallel strips attached to the surface of a smooth cylinder along the spanwise direction. The location of the upper strip varies in the range  $20^\circ \leq \alpha \leq 130^\circ$  (at  $10^\circ$  intervals) from the stagnation point (the coverage area  $\beta = 20^\circ$  and height  $t = 0.05D$  are constant); thus, in this section, the simulation cases are simply named  $P5 - \alpha$ . The total drag, lift force, and Strouhal number are compared in the next subsection, and typical cases are selected to visualize the flow around the cylinder and the wake structures. The distribution of circumferential force and spanwise correlation are then analyzed before the mean flow is discussed in detail.

##### A. Drag, lift, and Strouhal number

Vortex shedding is one of the characteristics of the flow around a cylinder, except at small Reynolds numbers ( $Re \leq 40$ ). The force around the cylinder changes periodically due to this vortex shedding. The force acting on the cylinder along the flow direction is called drag. The instantaneous drag oscillates periodically with time around the mean drag. The component acting on the cylinder along the transverse direction of the cylinder is called the lift force. As the incoming flow is completely symmetric with respect to the cylinder axis, the mean lift value is approximately zero. Still, the instantaneous lift varies with the same frequency as the periodic vortex shedding. The vortex shedding on each side of the cylinder causes anti-phase drag fluctuations, and

the amplitude of the fluctuating lift is obviously larger than that of the drag.<sup>51,52</sup> In this subsection, the mean drag force, root mean square lift force, and Strouhal number (vortex shedding frequency) of the PTC cylinders are discussed.

Figure 5 plots the dimensionless mean drag  $C_{d,ave} = \frac{F_{d,ave}}{\frac{1}{2}\rho U^2 DL}$ , dimensionless root mean square lift  $C_{l,rms} = \frac{F_{l,rms}}{\frac{1}{2}\rho U^2 DL}$ , and Strouhal number vs strip position  $\alpha$ ; the values for the smooth cylinder are also shown in the figure (solid line). It can be seen from Fig. 5 that the values  $C_{d,ave}$ ,  $C_{l,rms}$ ,  $St$  are different from those of the smooth cylinder when the upper strips are located at  $40^\circ \leq \alpha \leq 90^\circ$ . Because the flow is forced to separate without involving re-adhesion and secondary-separation when the strips are placed in this range, the primary vortex is formed closer to the cylinder, making the larger lift, drag forces, and vortex shedding frequency increase; meanwhile,  $St$  decreases. The maximum drag coefficient  $C_{d,ave} = 1.974$  of P5-60 is twice that of the smooth cylinder. The maximum lift coefficient  $C_{l,rms} = 0.627$  of P5-50 is approximately four times the value of 0.144 given by the smooth cylinder. That is because the leading edge of the strips is placed near the lowest location of the pressure distribution on the cylindrical surface. At this time, the thickness of the boundary layer is increasing due to the viscous effect of the flow, and encounter strips make the cylinder's pressure change rapidly. Then the boundary flow is forced to separate and spread far from both sides of the cylinder, forming the stronger vortex shedding in advance. Moreover, the change in the dimensionless force has an obvious slope at  $40^\circ \leq \alpha \leq 90^\circ$ , while the Strouhal number remains almost constant in this region at  $St \approx 0.15$ , indicating the frequency of vortex shedding is similar at this range. For

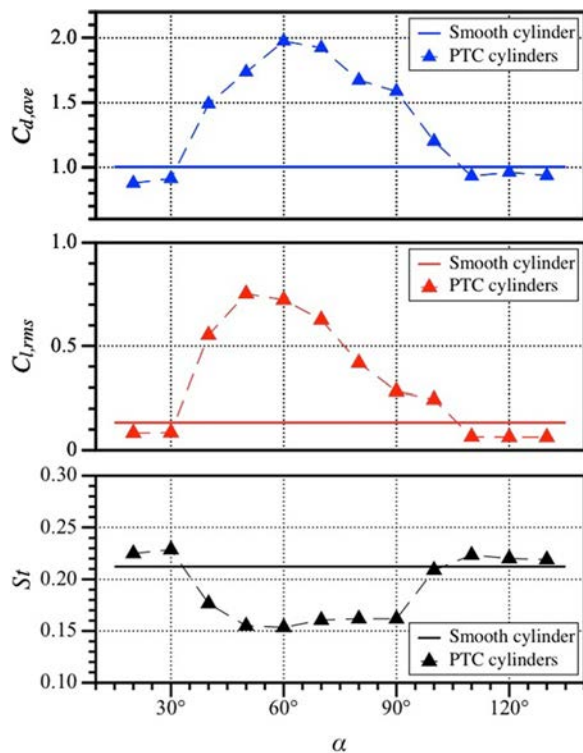


FIG. 5.  $C_{d,ave}$ ,  $C_{l,rms}$ , and  $St$  vs strip position.

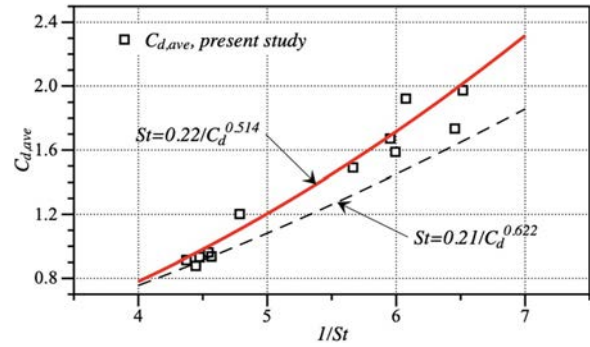


FIG. 6. Relationship between drag coefficient and Strouhal number.

P5-20 and P5-30, although the boundary layer separation occurred in advance, the drag and lift coefficients are smaller than the results for a smooth cylinder, while the Strouhal numbers are slightly larger. The reason might be due to the influence of the angle of the shear layer and the uniform flow around it; the separated fluid will reattach and separate again on the backside of the strips. For  $\alpha > 90^\circ$ , the formation of vortex has little change due to the separation has occurred before  $90^\circ$ , which has little effect on drag and lift.

Figure 6 depicts the relationship between the Strouhal number and mean drag coefficient. The red line is given by  $St = 0.22/C_{d,ave}^{0.514}$  (taken from Ref. 17), and the black dashed line indicates  $St = 0.21/C_{d,ave}^{0.622}$  (taken from Ref. 53), which were derived from many experimental results of the flow over bluff bodies. The current numerical calculation results are more in line with the equation derived by Igarashi,<sup>15</sup> including cylinders with and without strips.

The position of the strip in the range  $20^\circ \leq \alpha \leq 130^\circ$  affects the flow separation point by inducing changes in the flow force and vortex shedding frequency of the cylinder. Next, several typical cases are selected to analyze the flow over the cylinder in detail.

**B. Flow visualization and wake structure**

According to the effect of vortex generators on the flow over a cylindrical surface,<sup>17</sup> the flow around the cylinder can be divided into four patterns: pattern A (Strouhal number close to that of the smooth cylinder), patterns B and C (boundary undergoes a transition from laminar to turbulent flow), and pattern D (flow separation close to the disturbing element). The flow vorticity contours around the cylinders and the wake structure obtained in the present study are shown in Figs. 7–9.

The instantaneous vorticity contours of five typical cases and the smooth cylinder are shown in Fig. 7. The time-averaged streamline (black line in Fig. 7) shows the effect of the strip position on the separation point. The flow separation point of the cylinder without strips [Fig. 7(a)] occurs at around  $\phi = 85.68^\circ$ , as can be seen from the shear stress curves in Fig. 3. For P5-20, the incoming flow is forced to separate at  $\phi = 20^\circ$ , reattaches to the cylinder surface at  $\phi = 56.97^\circ$ , and separates a second time at  $\phi = 89.41^\circ$ . These angles are precisely calculated from the skin friction distribution in Fig. 10. The flow separation point has a delay of around  $4^\circ$  compared with that of the smooth cylinder. P5-30 exhibits similar phenomena, but the shear layer does not entirely attach to the cylindrical surface after the strip [see the

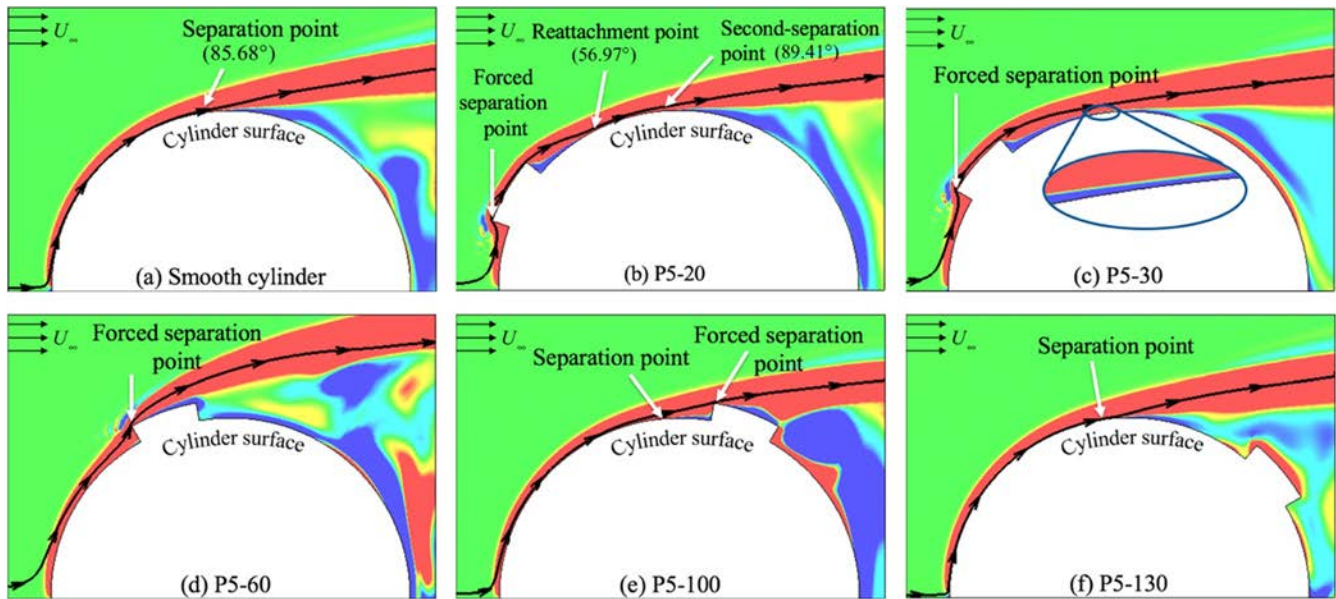


FIG. 7. Instantaneous vorticity contours. (a) Smooth cylinder, (b) P5-20, (c) P5-30, (d) P5-60, (e) P5-100, (f) P5-130.

magnified view of Fig. 7(c) and the skin friction curve of Fig. 10(c)]. Both P5-20 and P5-30 have similar Strouhal numbers to the smooth cylinder, so these two cases can be classified as pattern A. For P5-60, the shear layer and streamline are far away from the cylinder after the forced separation point, and there is no sign of reattachment. This can be recognized as pattern D as the Strouhal number is only about 0.15. A larger wake separation zone is formed by the position of the strip in

P5-60, resulting in an increased pressure force on the cylinder—this accounts for more than 95% of the total flow force in the present study. Thus, the pressure force caused by the large separation zone is the main factor for the increase in lift and drag shown in Fig. 5. For P5-100 and P5-130, the existence of strips has little or no effect on the mean streamline on the cylindrical surface, as shown in Figs. 7(e) and 7(f).

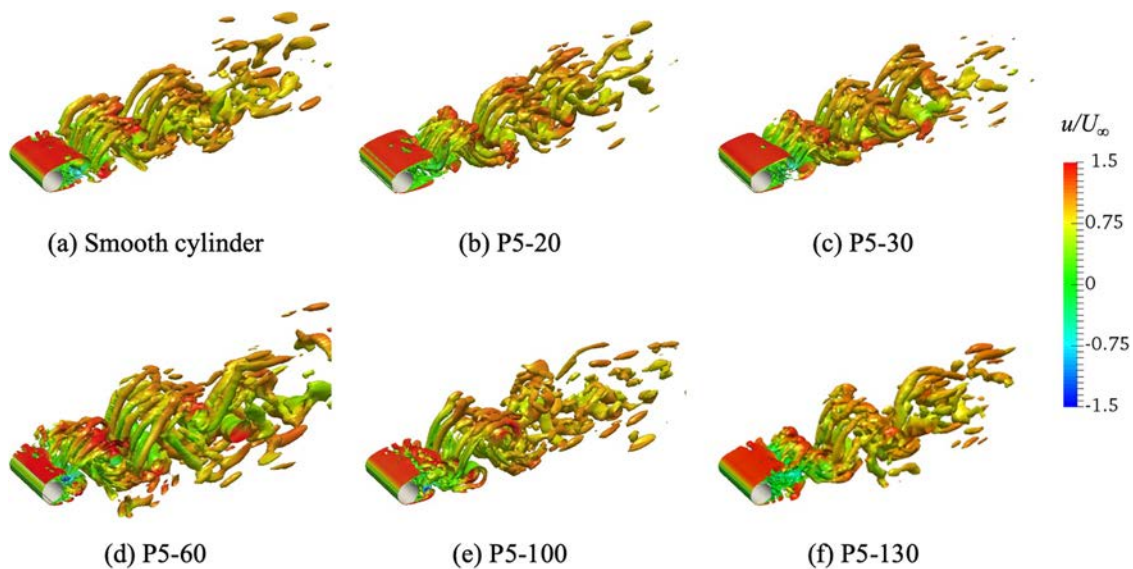


FIG. 8. Three-dimensional wake downstream of the cylinders. Instantaneous isosurface of the Q-criterion ( $Q = 0.8$ ) colored by isocontours of the streamwise velocity. (a) Smooth cylinder, (b) P5-20, (c) P5-30, (d) P5-60, (e) P5-100, and (f) P5-130.



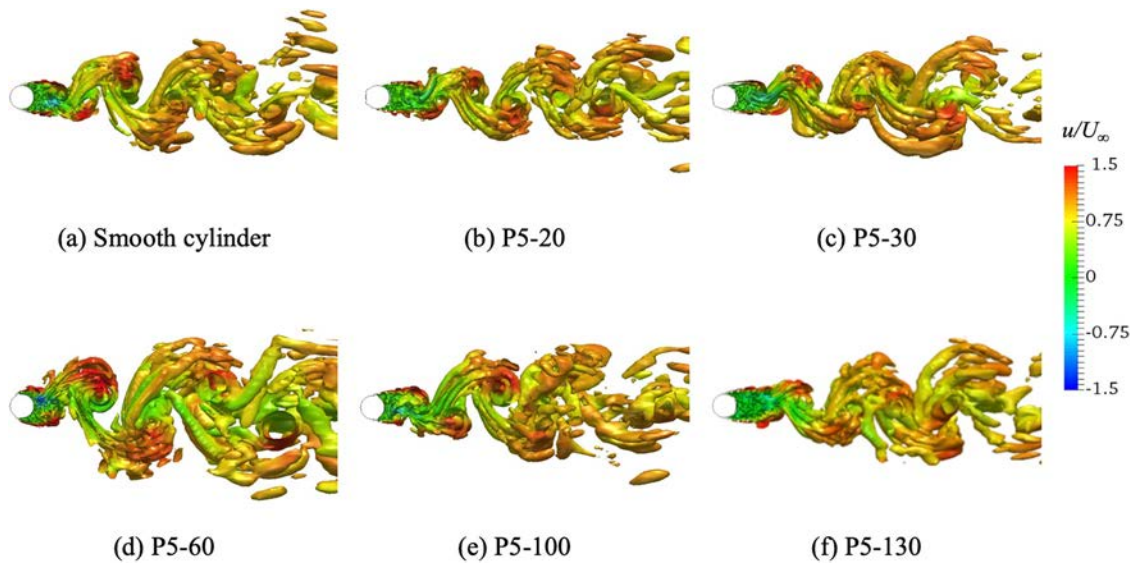


FIG. 9. View in y-direction of three-dimensional wake downstream of the cylinders. Instantaneous isosurface of the Q-criterion ( $Q = 0.8$ ) colored by isocontours of the stream-wise velocity. (a) Smooth cylinder, (b) P5-20, (c) P5-30, (d) P5-60, (e) P5-100, and (f) P5-130.

Figures 8 and 9 present a perspective view and y-view of the instantaneous three-dimensional wake structure of six cylinders (smooth, P5-20, P5-30, P5-60, P5-100, P5-130). All wakes have obvious three-dimensional characteristics, and alternate vortex shedding

can be distinguished downstream of the cylinders. From the three-dimensional view, the shear layer of pattern D in P5-60 is relatively short, and the primary vortex is formed near the cylinder. The wake vortex oscillates violently and the pressure downstream of the cylinder

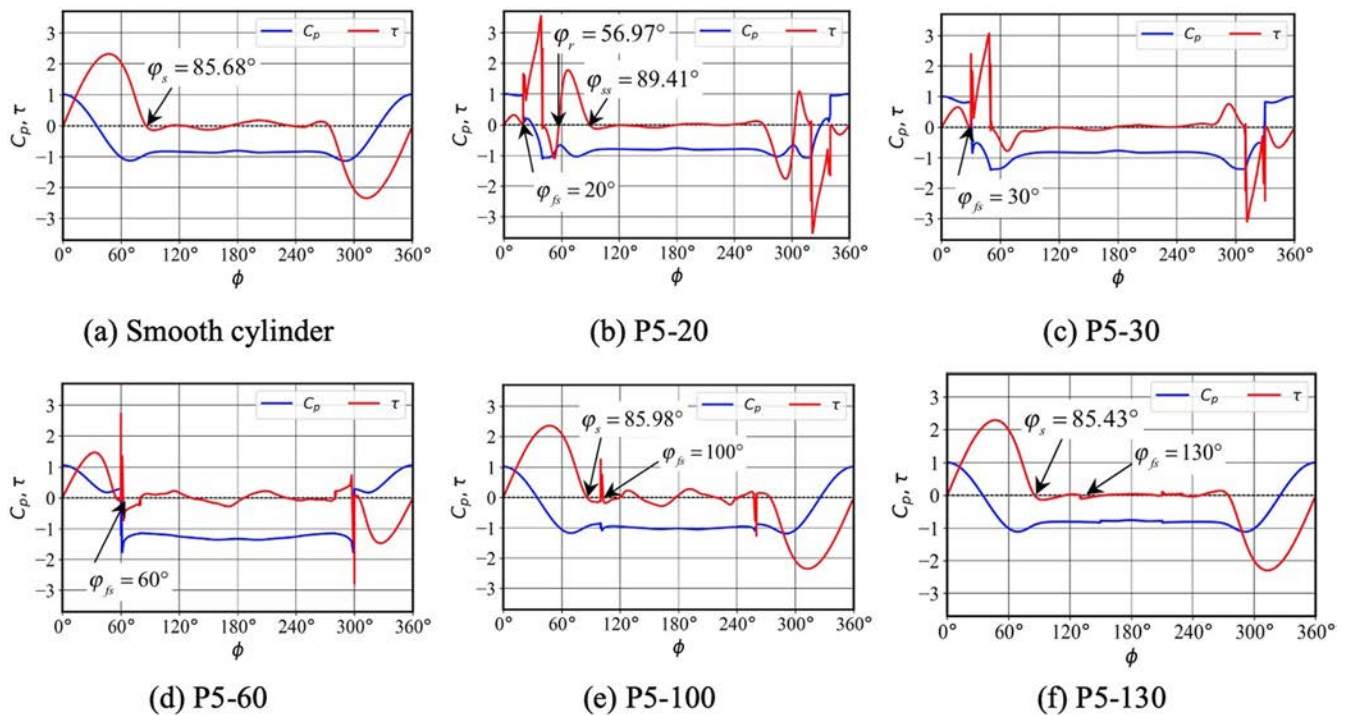


FIG. 10. Pressure and skin friction distribution. (a) Smooth cylinder, (b) P5-20, (c) P5-30, (d) P5-60, (e) P5-100, and (f) P5-130.

increases. This phenomenon is more evident from the side view [Fig. 9(d)]. The vortex structure in P5-60 is relatively large and is accompanied by a wider wake vortex, which prolongs the period of vortex shedding, corresponding to the Strouhal number analysis in Sec. IV A. Compared with the smooth cylinder, the structure and size of the wake vortex are reduced in cases P5-20 and P5-30, which shows that the PTC strips have a slight inhibitory effect on the hydrodynamic response of the cylinder. For P5-130, the vortices formed behind the cylinder are relatively small, but they expand as the flow develops downstream. It is speculated that, if the cylinder had some degrees of freedom, P5-20, P5-30, and P5-130 could suppress the cylinder's motion response. This subsection has examined the instantaneous flow around the cylinders and the wake structures. The strips induce patterns A and D. Pattern A has an inhibitory effect on the wake vortex, whereas pattern D will excite larger and wider vortex shedding. The pressure and skin friction distribution of these cases are discussed in Sec. IV C.

**C. Pressure and skin friction distribution**

According to the analysis of the drag, lift,  $St$ , and flow pattern of the PTC cylinders, this subsection analyzes the pressure and friction distribution of the PTC cylinders with  $\alpha = 20^\circ, 30^\circ, 60^\circ, 100^\circ, 130^\circ$ . In Fig. 10, the pressure and corresponding skin friction are plotted vs the peripheral angle  $\phi$  of the cylinder; the separation point ( $\phi_s$ ), forced separation point ( $\phi_{fs}$ ), reattachment point ( $\phi_r$ ), and second separation point ( $\phi_{ss}$ ) are marked. For P5-20, the pressure drop occurs sooner as a result of the strips, but quickly recovers. The shear stress increases significantly at the position of the strip, and then falls back to the reattachment point  $\phi_r = 56.97^\circ$  and second separation at  $\phi_{ss} = 89.41^\circ$ , which is also indicated in the flow around the cylinder in Fig. 7(b). For the P5-30 case, the pressure has a sharp drop and a slight rebound at  $\phi_s = 30^\circ$ . Moreover, the shear stress rises at first as the flow encounters the strip, then drops to zero at the rear edge. Note that no flow reattachment and second separation occurs for P5-30. For P5-60, the pressure and friction have a sharp change at  $\phi_{fs} = 60^\circ$ , but there is no rebound. As shown by the red line in Fig. 10(d), the strips can be regarded as “steps,” leading to turbulence and the formation of vortices. The sandpaper strips also appear to act as steps when the cylinder undergoes galloping in experiments,<sup>22</sup> but this speculation is due to the lack of force measurements. To be noted here, the boundary layer of P5-60 has developed to a certain thickness, and then strong vortices are formed when suddenly encountered obstacles and forced to separate. As a result, the recirculation length is shorter than in other cases, and the flow velocity changes more drastically downstream, which would be analyzed in detail in Sec. IV E. As shown in Figs. 10(e) and 10(f), the flow separation point on the cylinder surface is  $\phi_s = 85.98^\circ$  for P5-100 and  $\phi_s = 85.43^\circ$  for P5-130, which are very close to the value for the smooth cylinder. This indicates that the influence of the strips on the flow around the cylinder is relatively weak for P5-100 and P5-130.

At  $Re = 3900$ , the differential pressure drag caused by the pressure distribution on the cylindrical surface accounts for more than 95% of the total drag force; the contribution of friction to the resultant force is minimal and can usually be omitted. Therefore, the cylindrical surface pressures of the six cases are compared in Fig. 11. The pressure distribution curve of P5-60 is the most different from that of the smooth cylinder, without any overlap. The base suction downstream

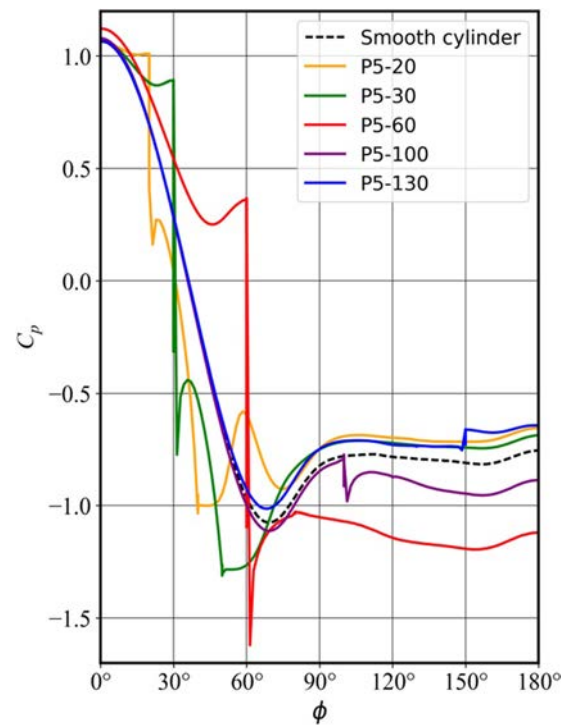


FIG. 11. Comparison of the pressure distribution at various strip positions.

of the cylinder has dropped by about 60%, which is the main reason for the larger drag coefficient of P5-60 in Fig. 5, according to the strong correlation between base suction and pressure.<sup>54</sup> The pressure distributions of P5-20 and P5-30 change significantly before  $\phi = 40^\circ$  and  $\phi = 50^\circ$ , but the strips have a minor effect downstream of the cylinder, and the pressure gradually approaches the smooth cylinder pressure distribution curve. For P5-100, the pressure distribution almost entirely coincides with that of the smooth cylinder before the location of the strips. At  $\phi = 100^\circ$ , i.e., the front edge of the PTC strips, the pressure drops slightly and remains lower. The pressure distribution curve of P5-130 shows that the pressure downstream of the cylinder is close to that of P5-30, and then there is a significant increase at the position of the strips ( $\phi = 130^\circ$ ) that decreases the drag compared with the case of a smooth cylinder.

**D. Spanwise lift correlation**

We have seen that the lift of the cylinder is affected by vortex shedding. Nevertheless, except for some situations in laminar shedding flows, in-phase vortex shedding does not occur in the spanwise direction of the entire cylinder, such as in transitional and turbulent vortex shedding.<sup>55</sup> Therefore, in this subsection, we study the correlation of the fluctuating lift forces between sections along the cylinder's spanwise direction. The lift change along the cylinder span is quantified by the axial correlation coefficient, which is defined as

$$R = \frac{\sum (F_l - \bar{F}_l)(F'_l - \bar{F}'_l)}{\sqrt{\sum (F_l^2 - \bar{F}_l^2)(F'^2_l - \bar{F}'^2_l)}}, \tag{8}$$

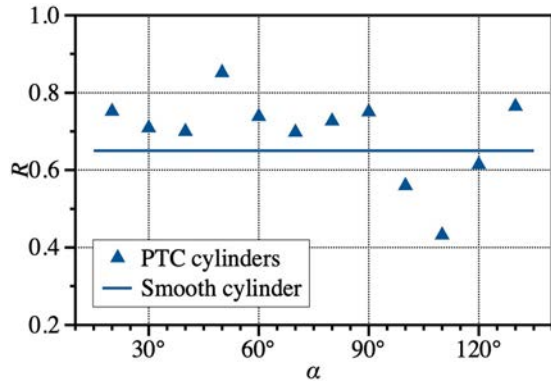


FIG. 12. Correlation coefficient  $R$  of two ends of cylinders.

where  $F_l$  represents the lift coefficient of the cylinder’s end section and  $F'_l$  is the lift coefficient of other sections along the cylinder span.  $\overline{F_l}$  and  $\overline{F'_l}$  are the corresponding time-averaged lift coefficients.

The correlation between the two ends of the cylinder is plotted in Fig. 12. The results for the smooth cylinder are also shown. When the strips are placed before  $\alpha = 90^\circ$ , the lift correlations are improved, which indicates that strips at these positions increase the flow consistency along the cylinder spanwise direction and weaken the three-dimensional effect. However, the strips might destroy the regularity of the wake formation, causing the correlation to decrease, when placed behind the cylinder main section, as for P5-110. The best correlation between cylinder ends occurs for P5-50, and the worst is for P5-110. Recall that the length of the cylinder is  $\pi D$  in the present study. It can be speculated here that when the lift correlation analysis is adopted in longer or flexible cylinders, more intuitive results could be obtained, such as second-order displacement or structural damage when the lift correlation is low. More details about the change in the lift correlation  $R$  along the spanwise direction for the smooth cylinder, P5-50, and P5-110 are given in Figs. 13 and 14. As can be seen from Fig. 13, the lift correlation coefficients decrease as the cross-sectional distance increases, and this downward trend is most significant for P5-110. For P5-50, the correlation coefficient remains close to 0.85 after the middle

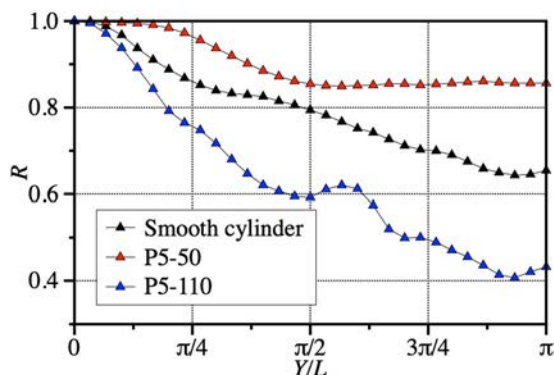


FIG. 13. Correlation coefficient  $R$  of the sectional lift force.

section. In Fig. 14, the contours of section lift with respect to time are plotted in the  $y$ - $t$  plane. First, the axial continuity of the lift in Fig. 14(c) is worse than that in Figs. 14(a) and 14(b), which illustrates the same fact as Fig. 13: the axial correlation of P5-110 is worse than in the other cases. Additionally, the period of fluctuating lift for P5-110 is similar to that of the smooth cylinder, while the period of fluctuating lift for P5-50 is larger. This further verifies the analysis of the shedding frequency in Sec. IV A. Figures 14(d) and 14(e) show the instantaneous vortex structures corresponding to Fig. 14(c) at different times. The alternately shedding Karman vortex street can be identified in Fig. 14(e), but the vortex shedding in Fig. 14(d) is not very regular. This reveals the greater instability of the flow around the P5-110 cylinder.

### E. Mean flow and turbulence statistics

In this subsection, the average flow and turbulence statistics of PTC cylinders are analyzed in detail. First, it is necessary to consider the convergence of the data obtained from our simulations, which is closely related to the total calculation time. Previous tests have examined 7–131 vortex shedding cycles.<sup>34,45,48,56</sup> When more than 40 vortex shedding cycles are considered, the first- and second-order flow field statistics are generally stable.<sup>7</sup> Therefore, the current study simulates 52 vortex shedding cycles for statistical analysis of the mean flow and turbulence.

The recirculation length  $l_{re}$  in the wake region of the flow is an important factor in the statistical analysis of the mean flow of the cylinder.<sup>10,34</sup> For the PTC cylinders and the smooth cylinder, these values are plotted in Fig. 15. Clearly, the recirculation zone of PTC cylinders with  $40^\circ \leq \alpha \leq 100^\circ$  is significantly smaller than in other cases, indicating that attaching strips in this area makes vortex shedding easier. We compare the details for P5-30, P5-60, P5-130, and the smooth cylinder, and show the mean streamwise velocity of their cylindrical wake centerline in Fig. 16. P5-60 has a shorter recirculation zone and lower streamwise flow velocities, with the flow velocity moving monotonously toward the incoming flow velocity  $U_\infty$ .

The isocontour maps of the first- and second-order statistics are displayed in Fig. 17. These results provide a complete perspective of the information in the calculation domain ( $x = 5D$ ). Figure 17 shows that each case has an apparent recirculation zone. The smallest recirculation zone occurs for P5-60, and the largest is for P5-130. The maps of streamwise velocity  $u'$  and  $u'u'$  show the symmetric shear layers. The maximum  $v'v'$  values are located on the wake centerline. The shapes of the  $v'$  and  $u'v'$  maps are antisymmetric, especially  $u'v'$ , which looks like a butterfly with two extrema on each side of the wake centerline. P5-60 gives the most unusual isocontour maps. The shear layers are wider and thicker;  $u'$  exhibits more velocity loss because of large-area flow separation; the maximum  $u'u'$  value is symmetric on each side of the wake centerline; and the maximum  $v'v'$  value is closest to the cylinder; and the  $u'v'$  map has the largest “wings.” This analysis, however, is a qualitative understanding of the average flow velocity of the fluid around the cylinder. For quantitative analysis, we examine P5-60 and the smooth cylinder, and perform statistical analysis of the first- and second-order turbulence in the wake region ( $x/D = 0.58, 1.06, 1.54, 2.02, 3, 5$ ).

Figure 18 shows the mean velocity profiles at six  $x$ -locations downstream of the cylinder, including streamwise velocities and normal velocities. As shown in Fig. 18(a), U-shaped streamwise velocities

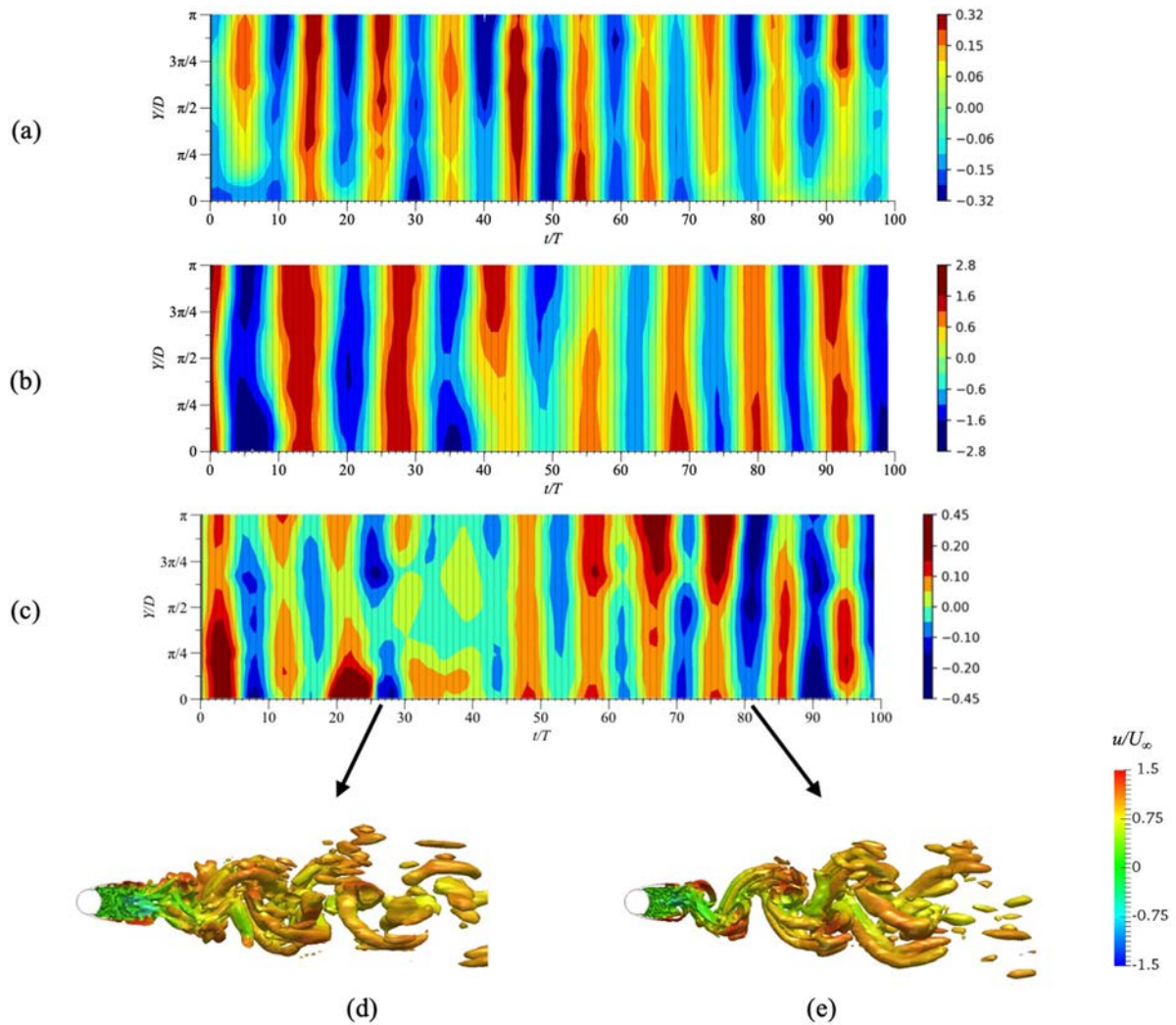


FIG. 14. Instantaneous sectional lift contour and instantaneous wake structure. (a) Smooth cylinder, (b) P5-50, and (c) P5-110; (d) and (e) instantaneous wake structure of P5-110.

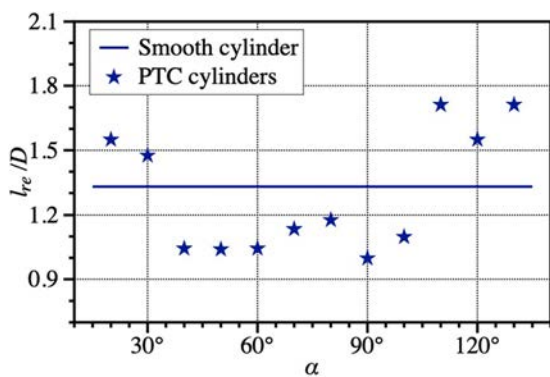


FIG. 15. Recirculation length.

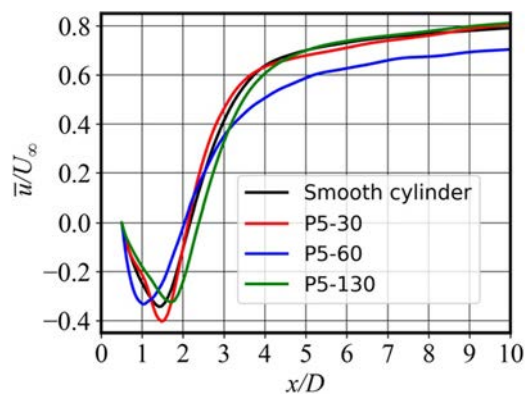


FIG. 16. Mean streamwise velocity in the wake centerline of the cylinders.

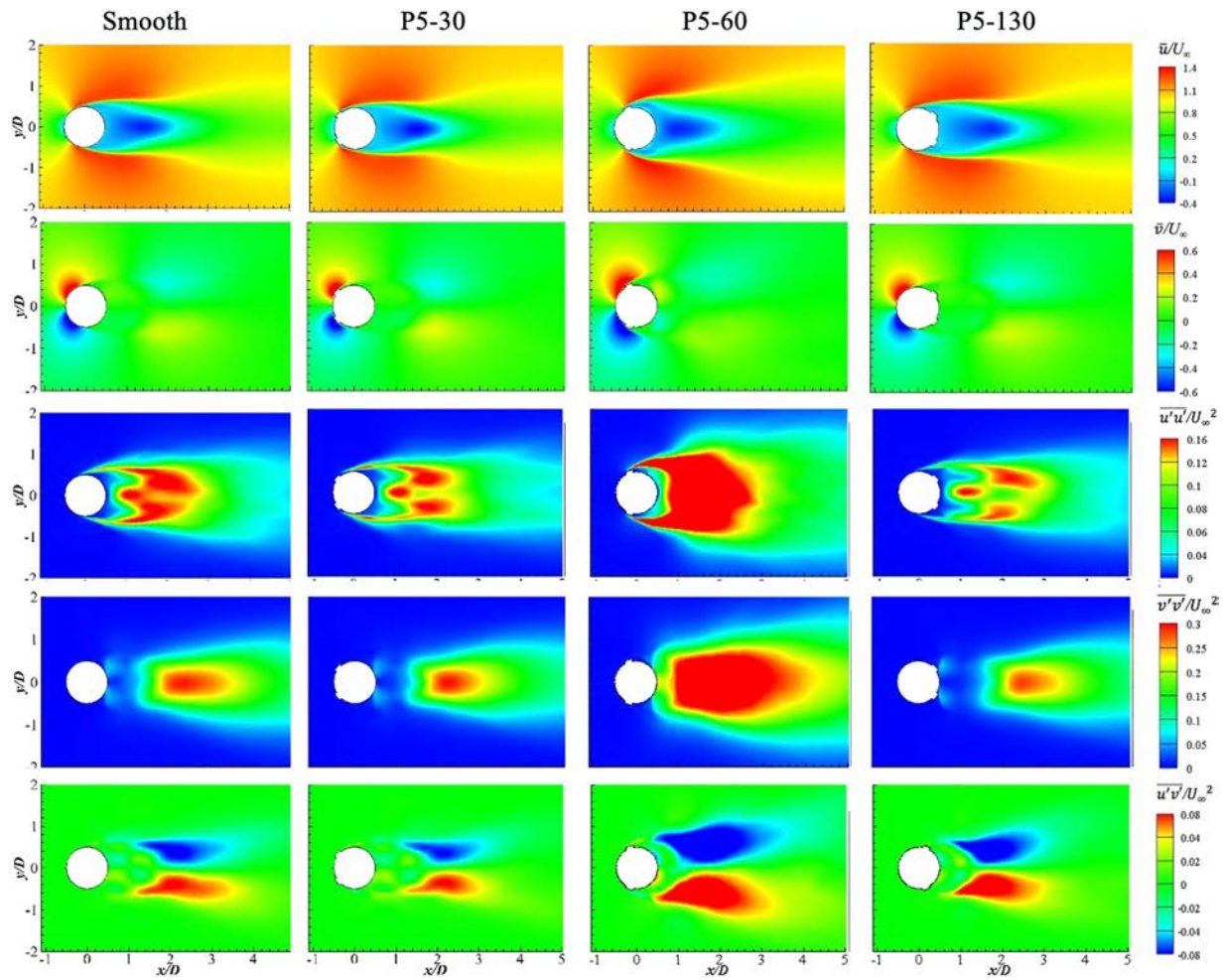


FIG. 17. Isocontour map of the first- and second-order statistics of smooth, P5-30, P5-60, and P5-130 cylinders; from top to bottom:  $u, v, u', v',$  and  $u'v'$  normalized according to  $U_\infty$  or  $U_\infty^2$ .

occur near the cylinders, and these evolve to V-shaped profiles further downstream. A strong velocity deficit in the wake area occurs for both the smooth cylinder and P5-60. This velocity deficit comes from the low-velocity zone induced by the cylinder surface boundary layer and the flow separation. The two low-velocity zones quickly blend together downstream and converge toward the centerline, forming a unified wake loss zone. This velocity deficit continues further downstream. Due to the disturbance effect of the strips, flow separation occurs earlier in P5-60 and the shear layer spreads more widely to both sides of the cylinder. As can be seen from Fig. 18(a), compared with the smooth cylinder, the range of velocity loss is broader, and the streamwise velocity recovers slower at a position further downstream. Figure 18(b) shows that the average velocity in the transverse direction of P5-60 has a large gap close to the cylindrical wall. Still, the velocity is quickly restored further downstream, indicating that the strips' influence is weakening.

The variance and covariance of the flow velocity fluctuations at six positions in the wake of the smooth and P5-60 cylinders are plotted

in Fig. 19, including streamwise and normal directions. A pair of prominent peaks caused by the shear layer transition appear at  $x/D = 0.58$ , invariant with respect to streamwise velocity fluctuations [Fig. 19(a)]. The contribution to the peak is more evident in the case of P5-60, because the wider shear layer forms more extensive primary vortices. Further downstream of the cylinder, the primary vortex formed by the shear layer becomes strongly agitated. It gradually covers the pair of peaks at the position of the primary vortices, and this situation occurs earlier for P5-60 than for the smooth cylinder. The recirculation length ( $L_{re} \approx 1.04$  for P5-60 and  $L_{re} \approx 1.41$  for the smooth cylinder) is an important factor for the mean flow statistical analysis and is the main reason for the difference in the variance and covariance of the velocity fluctuations at  $x/D = 1.06, 1.54$ . The covariance of the velocity fluctuations [Fig. 19(b)] presents an anti-symmetric distribution. The values for P5-60 are very different from those for the smooth cylinder at positions before  $x/D = 3$ , but quickly return to normal downstream. The variance of the normal velocity profiles resembles a hillside [Fig. 19(c)], and as the flow moves

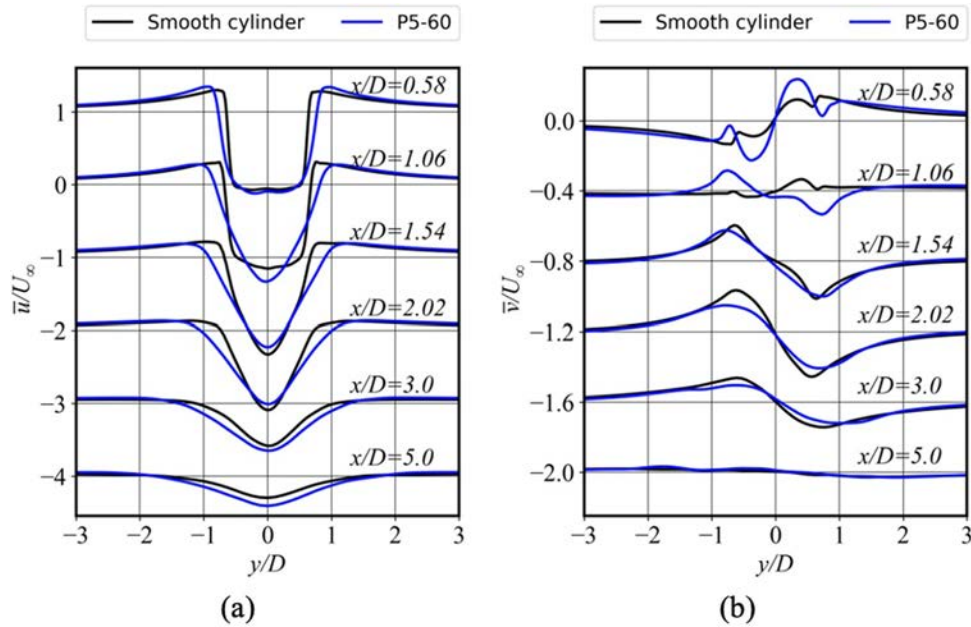


FIG. 18. Mean velocity at six locations downstream of the smooth cylinder and P5-60. (a) Streamwise velocity and (b) normal velocity.

downstream, the shapes become more and more gentle. In summary, all the distributions of the first- and second-order statistics shown in Figs. 18 and 19 correspond to the features of the isocontour map in Fig. 17.

V. IMPACT OF STRIP COVERAGE AREA AND THICKNESS AT  $\alpha = 60^\circ$

This section studies the influence of the coverage area and height of the strips on the flow around the cylinder. Based on the results presented in Sec. IV, we fix  $\alpha = 60^\circ$  throughout this analysis.

A. Impact of strip coverage area

With the leading edge of the strips fixed at  $\alpha = 60^\circ$ , Fig. 20 compares the drag, lift force, and Strouhal number of cases with different strip coverage ( $\beta$  from  $5^\circ$ – $100^\circ$ ). The highest drag and lift force coefficients appear for P5-60-5 and then decrease slightly as the coverage increases. Note that the changes in the lift and drag coefficients are identical. The force fluctuation may be caused by the trailing edge of the strip colliding with the vortex shedding. The Strouhal number is around 0.15 for all cases of P5-60, indicating that the formation of the

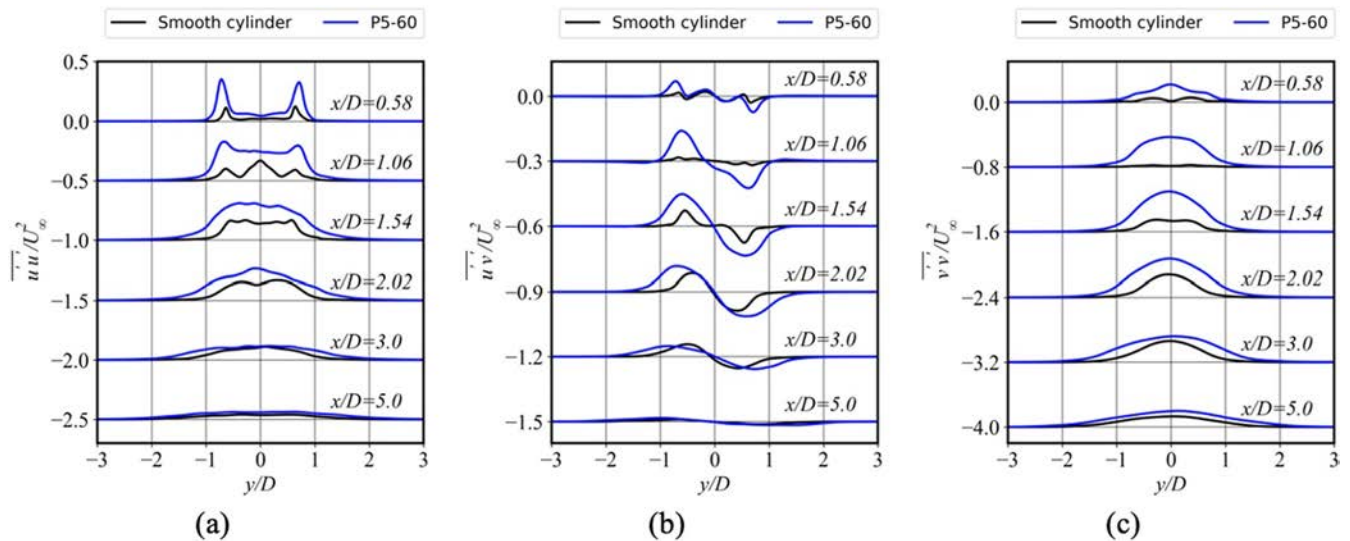


FIG. 19. Velocity fluctuations at six locations downstream of the smooth cylinder and P5-60. (a) Streamwise variance, (b) covariance of the velocity fluctuation, and (c) variance of the normal velocity.

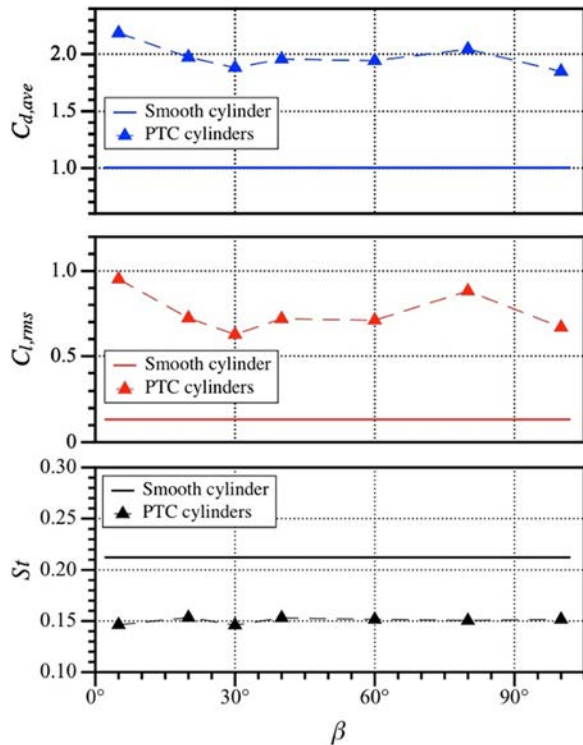


FIG. 20.  $C_{d,ave}$ ,  $C_{l,rms}$ ,  $St$  vs strip coverage.

vortex is little affected by the strip width when the flow is separated forcefully.

The pressure and skin friction distribution of P5-60-5, P5-60-20, and P5-60-100 are revealed in Fig. 21. The curves are almost the same before  $\phi = 60^\circ$ , both for pressure and skin friction. The pressure distribution starts to deviate at the rear edge of the strips, where the pressure in the case of P5-60-5 is lower than in other cases, and the curve for P5-60-100 is similar to that for P5-60-20, except for a sudden rise at  $\phi = 100^\circ$ . Moreover, the turbulence occurs earlier for the narrowest strips, as can be seen from the skin friction results in Fig. 21(b). The

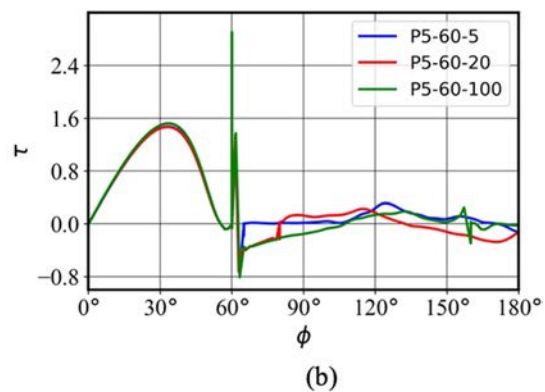
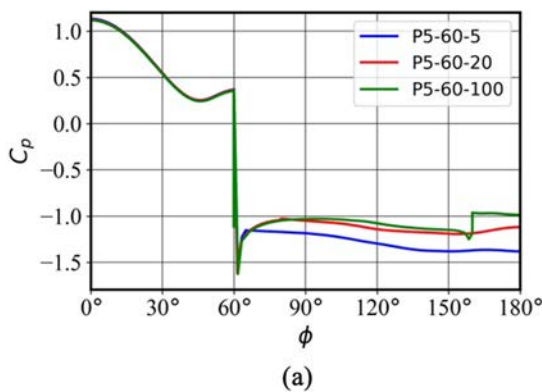


FIG. 21. Comparison of the pressure and skin friction distribution for cylinders with various strip coverages. (a) Pressure distribution and (b) skin friction distribution.

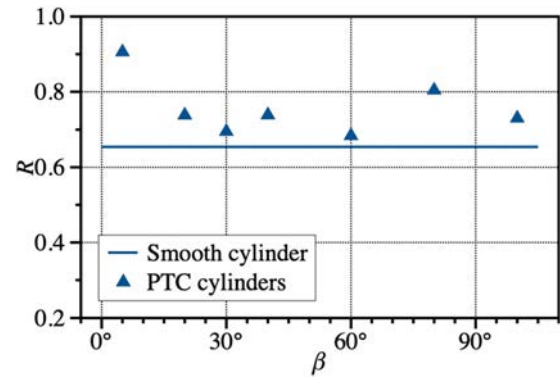


FIG. 22. Correlation coefficient  $R(0, y)$  for cylinders with various strip coverages.

strips at this position are like a baffle, blocking the path of the fluid and forcing the boundary layer to separate, and when the baffle is thinner (that is, the smaller the coverage), the flow particles will collectively move away from the cylinder and have more space behind the thin baffle to develop into turbulence after the fluid is triggered to separate. At this time, the spanwise lift correlation is also better, and if the baffle covers a wide area of the cylindrical surface, that part of the flow particles could adhere to the surface of the strips, and turbulence would occur later. The lift correlation between the two ends of the cylinders for different coverage cases is given in Fig. 22. The trend is highly consistent with that of the drag and lift coefficients in Fig. 20. All cases exhibit good correlation, with a maximum of around  $R = 0.9$  in the narrowest strips and a minimum of 0.684 for P5-60-60. The sectional lift correlation and instantaneous lift correlation contours along the spanwise direction of the highest and lowest points of Fig. 22 are presented in Figs. 23(a) (for P5-60-5) and 23(b) (for P5-60-60). The periodic changes in the contours indicate that the lift force shedding frequencies are very similar, which means that similar vortex shedding frequencies will occur in each case. The correlation for P5-60-60 has a more pronounced inflexion point around two-thirds of the distance from the end of the cylinder, as shown in Fig. 23(b).

The results in this subsection show that the coverage of the strips has little effect on the flow. The narrowest strips, P5-60-5, result in higher lift and drag and better spanwise correlation.

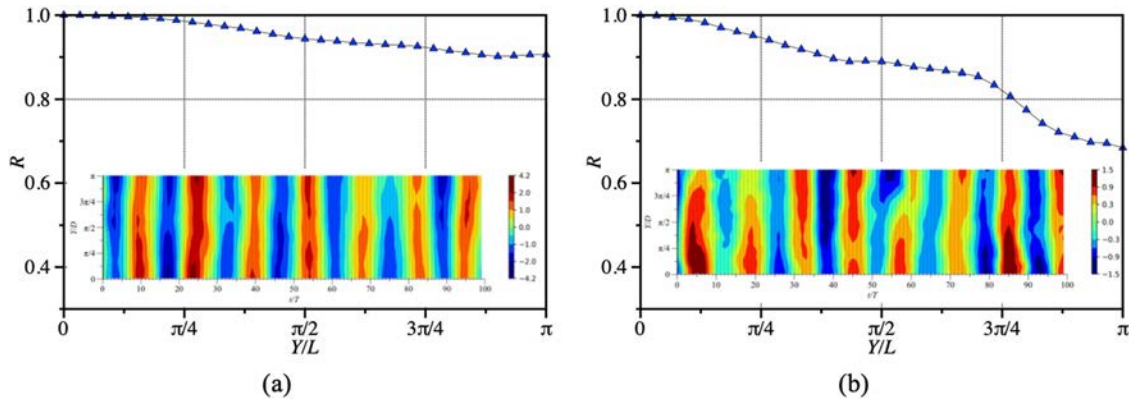


FIG. 23. Instantaneous lift correlation contours along the spanwise direction. (a) P5-60-5, (b) P5-60-60.

**B. Impact of strip thickness**

The effect of the strip height ( $t = 0.01D, 0.03D, 0.05D$ ) on the flow characteristics is considered in this subsection for  $\alpha = 60^\circ$  and  $\beta = 20^\circ$ . The drag, lift force coefficient, and Strouhal number are shown in Fig. 24. The coefficient of force decreases as the strip height decreases, getting progressively closer to the result for a smooth cylinder. This indicates that flow pattern D is transforming to pattern A, especially for P1-60-20, where the effect of the strips on the fluid flow

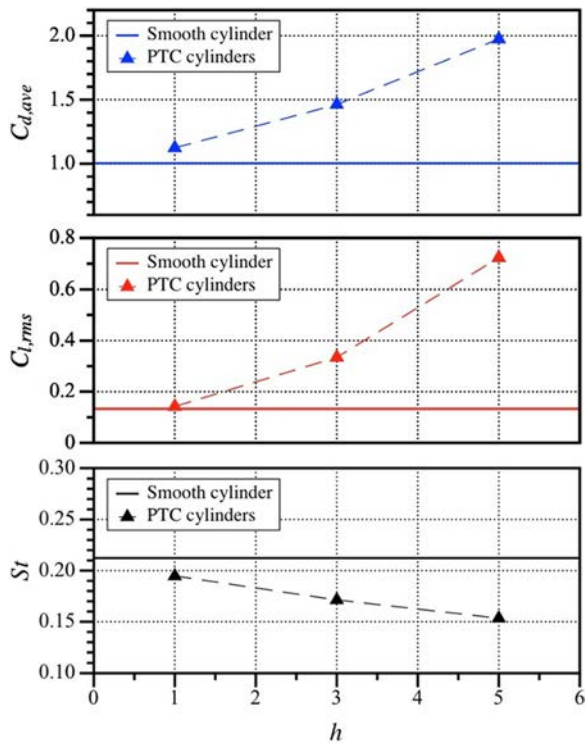


FIG. 24.  $C_{d,ave}$ ,  $C_{l,rms}$ ,  $St$  vs strip height.

is very small. Following the approximate method of Pohlhausen of boundary-layer theory,<sup>57</sup> the height of the strips for P1-60-20 at  $\alpha = 60^\circ$  is less than the boundary layer thickness, which might induce pattern B or C (larger Strouhal number and smaller drag force compared with the smooth cylinder) if the Reynolds number falls into the range  $2 \times 10^4 \leq Re \leq 5 \times 10^5$  in this region.<sup>16–19</sup> There is no sign of pattern B or C, possibly because the Reynolds number in the current study is smaller than that considered in the previous research.

The instantaneous vorticity contours of three cases are shown in Fig. 25. The time-averaged streamline (black line in Fig. 25) shows the effect of strip thickness on the separation point. For P1-20-60, the strip height has a minor effect on the flow over the cylinder, even without involving the forced separation at the front edge of the strips. For P3-20-60 and P5-20-60, the flow separates at  $\phi = 60^\circ$ , and neither reattachment nor secondary separation occurs downstream. The outward expansion of the flow becomes more obvious as the strip thickness increases [see Figs. 25(b) and 25(c)], which will also affect the formation of the primary vortex.

Figures 26 and 27 present the perspective and y-views of the instantaneous three-dimensional wake structure of three cylinders (P1-60-20, P3-60-20, P5-60-20). The wakes all have obvious three-dimensional characteristics, and Karmen vortices can be distinguished downstream of the cylinder in the y-view. Compared with the wake structure for the smooth cylinder [Figs. 8(a) and 9(a)], there is no obvious difference in vortex size or distance to the cylinder for P1-60-20. Moreover, for P3-60-20, the vortex shedding is more extensive and closer to the cylinder. The vortex structure of P5-60-20 has been analyzed in Sec. IV B. In short, as the height of the strips increases, the vortex spreads to both sides of the cylinder, accompanied by an increase in the size of the vortex and a closer spacing.

The pressure and skin friction distribution of three cylinders are depicted in Fig. 28. The results for the smooth cylinder are also presented as a black dashed line. Each flow condition exhibits a sudden change when encountering the strips, regardless of their height. The presence of thinner strips seems to have a greater impact on the surface friction of the PTC cylinders, but no lift and drag changes for P1-60-20 are apparent because the friction force is a small percentage of the total force. Additionally, the strips in the case of P1-60-20 only



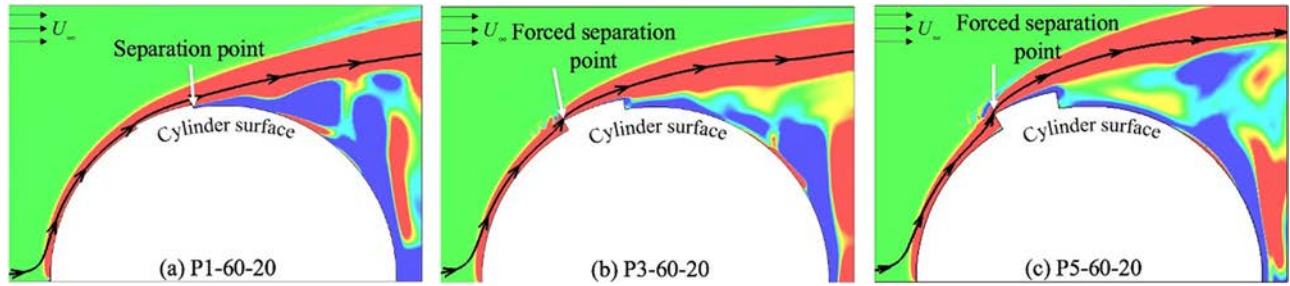


FIG. 25. Instantaneous vorticity contours. (a) P1-60-20, (b) P3-60-20, (c) P5-60-20.

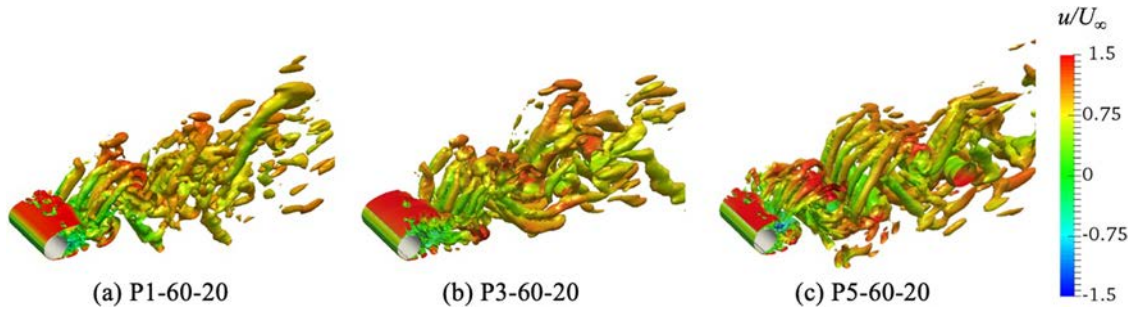


FIG. 26. Three-dimensional wake downstream of the cylinders. Instantaneous isosurface of the Q-criterion ( $Q = 0.8$ ) colored by isocontours of the streamwise velocity. (a) P1-60-20, (b) P3-60-20, and (c) P5-60-20.

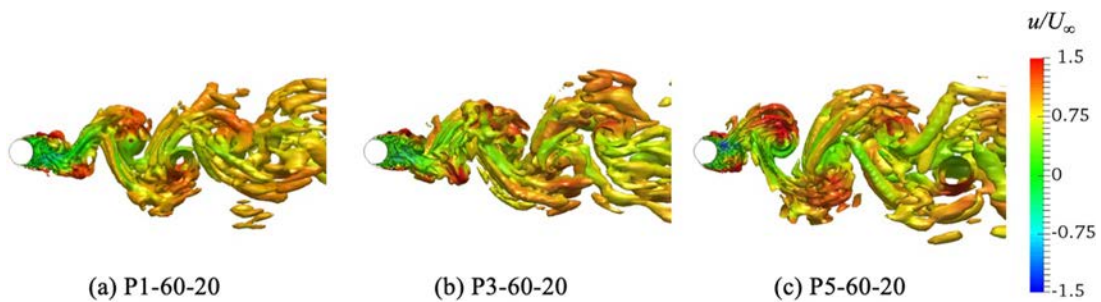


FIG. 27. View in y-direction of three-dimensional wake downstream of the cylinders. Instantaneous isosurface of the Q-criterion ( $Q = 0.8$ ) colored by isocontours of the streamwise velocity. (a) P1-60-20, (b) P3-60-20, and (c) P5-60-20.

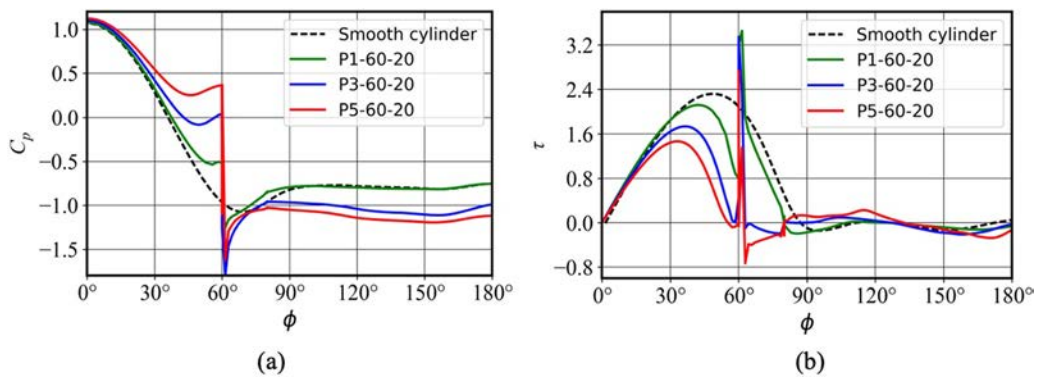


FIG. 28. Comparison of the skin friction and pressure distribution for cylinders with various strip heights. (a) Pressure distribution and (b) skin friction distribution.

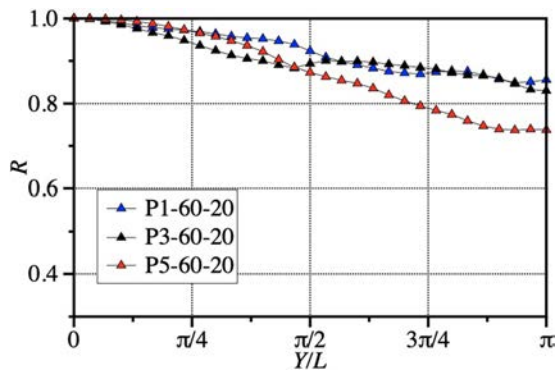


FIG. 29. Correlation coefficient  $R$  of the sectional lift.

change the separation point from  $85.68^\circ$  to  $80^\circ$  [see Fig. 28(b)], which has little effect on the formation of vortices.

The lift force correlations for the cylinder sections are shown in Figs. 29 and 30. It can be seen from Fig. 30 that the lift correlations of all three cases are better than that of the smooth cylinder. The best correlation occurs in P1-60-20 as the strip height is less than the boundary layer thickness. For P1-60-20 and P3-60-20, the curves tend to approach one another from the middle section of the cylinder. Figure 30 presents the instantaneous lift correlation profiles corresponding to

the curves in Fig. 29. The most considerable periodic change occurs for P5-60-20, which indicates faster vortex shedding. The main reason why the correlation of P5-60-20 is slightly lower than for the other cases is that there is a lag in the cross-sectional lift phase as the profile is slightly inclined rather than straight, as can be seen in Fig. 30(c). The results presented in this section suggest that the height of the strips has more of an influence on the flow around the cylinder than the strips' coverage.

VI. CONCLUSIONS

This paper has described the characteristics of the flow around cylinders with strips symmetrically attached to both sides. The flow characteristics were studied at  $Re = 3900$  for various strip positions, coverage, and thickness. The lift, drag,  $St$ , wake, pressure and skin friction distributions, mean flow and turbulence statistics, and lift correlation have been analyzed; the following conclusions can be drawn:

- (1) Two flow modes, patterns A and D, can be identified from the vortex enhancement and suppression of the flow around PTC cylinders. The Strouhal number of pattern A is very close to the response of the smooth cylinder. The lift and drag force in pattern D are significantly higher, and the Strouhal number decreases to around 0.15, accompanied by the free shear layer spreading outward and an increase in the number of wake vortices. The critical position for the transition from pattern A to pattern D is  $\alpha = 30^\circ$ .

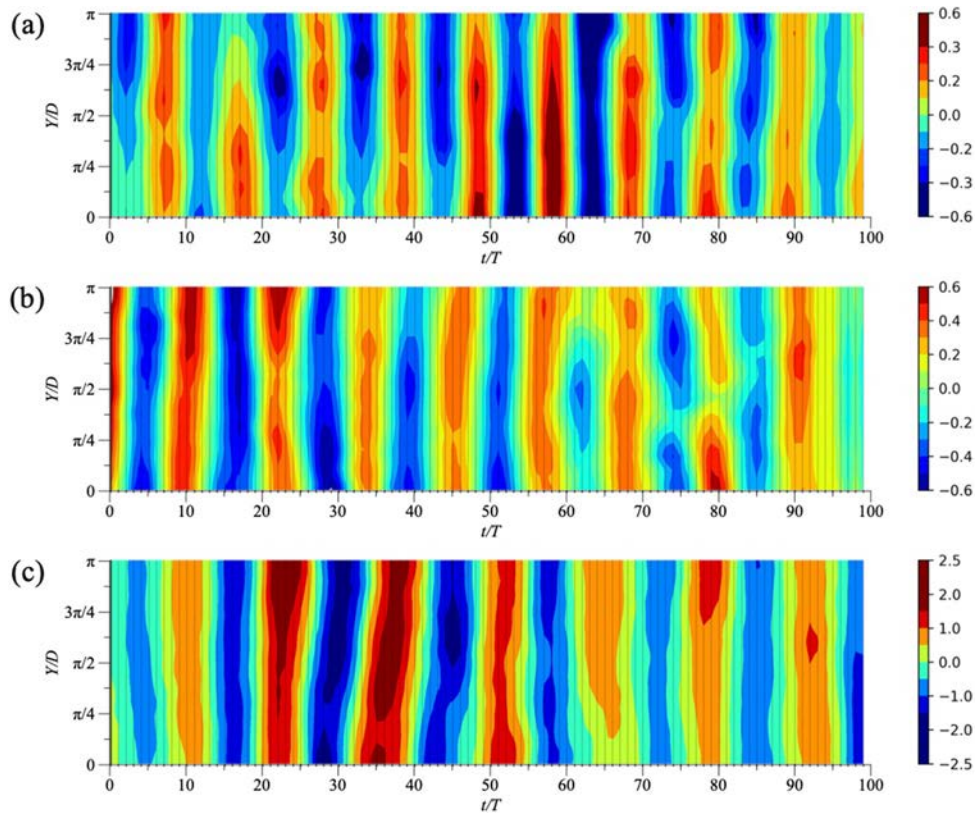


FIG. 30. Instantaneous sectional lift contours along the spanwise direction. (a) P1-60-20, (b) P3-60-20, and (c) P5-60-20.

- (2) In the statistical analysis of the mean velocity, the P5-60-20 cylinder exhibits a greater disturbance near the cylinder, which separates the flow in advance and moves away from the cylinder. This causes a greater velocity deficit, which gradually recovers further downstream.
- (3) For cylinders with strips located before  $\alpha = 90^\circ$ , the lift correlation of the cylinder sections is better than that for the smooth cylinder. However, when located at the trailing edge of the cylinder, the strips affect the free shear layer and vortex structure formation, causing the correlation to decrease, except for P5-130-20. Cylinders with low lift correlation may suffer from irregular vortex shedding and wake structures because of the instability.
- (4) When the leading edge of the strips is fixed at  $\alpha = 60^\circ$ , change in the coverage has little effect on the flow. However, the current study has found that the narrowest strips have the smallest Strouhal number and the best lift correlation. Moreover, the trend in the span correlation for P5-60 is the same as for the lift and drag force.
- (5) At the Reynolds number considered herein, when the front edge of the strips is fixed at  $\alpha = 60^\circ$  and the coverage area is  $\beta = 20^\circ$ , a turbulent boundary layer (patterns B and C) is not induced, regardless of whether the strip height is greater or less than the boundary layer thickness. When  $t = 0.01D$ , the impact on the flow is negligible, and the flow pattern can be recognized as pattern A. In this case, the correlation of the lift coefficients is significantly better than for other heights.

In subsequent research, the FIV response of the PTC cylinders will be further studied and compared with that of a smooth cylinder to analyze the mechanism of suppression or excitation. This is expected to provide further support for the theory and engineering applications.

## ACKNOWLEDGMENTS

This work was supported by the National Key Research and Development Program of China (Nos. 2019YFB1704200 and 2019YFC0312400) and National Natural Science Foundation of China (No. 51879159), to which the authors are most grateful.

## DATA AVAILABILITY

The data that support the findings of this study are available from the corresponding author upon reasonable request.

## REFERENCES

- <sup>1</sup>C. Mathis, M. Provansal, and L. Boyer, "The Benard-Von Karman instability: An experimental study near the threshold," *J. Phys. Lett.* **45**(10), 483–491 (1984).
- <sup>2</sup>B. Kumar and S. Mittal, "Prediction of the critical Reynolds number for flow past a circular cylinder," *Comput. Methods Appl. Mech. Eng.* **195**, 6046–6058 (2006).
- <sup>3</sup>C. H. K. Williamson and A. Roshko, "Vortex formation in the wake of an oscillating cylinder," *J. Fluids Struct.* **2**, 355–381 (1988).
- <sup>4</sup>H. Jiang, "Separation angle for flow past a circular cylinder in the subcritical regime," *Phys. Fluids* **32**(1), 014106 (2020).
- <sup>5</sup>H. Zhang, U. Fey, B. R. Noack, M. König, and H. Eckelmann, "On the transition of the cylinder wake," *Phys. Fluids* **7**(4), 779–794 (1995).
- <sup>6</sup>W. W. Zhao and D. C. Wan, "Numerical study of 3D flow past a circular cylinder at subcritical Reynolds number using SST-DES and SST-URANS," *Shuidonglixue Yanjiu Yu Jinzhan/Chin. J. Hydrodyn. Ser. A* **31**(1), 1–8 (2016).
- <sup>7</sup>J. Franke and W. Frank, "Large eddy simulation of the flow past a circular cylinder at  $Re_D = 3900$ ," *J. Wind Eng. Ind. Aerodyn.* **90**(10), 1191–1206 (2002).
- <sup>8</sup>M. H. Wu, C. Y. Wen, R. H. Yen, M. C. Weng, and A. B. Wang, "Experimental and numerical study of the separation angle for flow around a circular cylinder at low Reynolds number," *J. Fluid Mech.* **515**, 233–260 (2004).
- <sup>9</sup>C. Xu, L. Chen, and X. Lu, "Large-eddy and detached-eddy simulations of the separated flow around a circular cylinder," *J. Hydrodyn.* **19**(5), 559–563 (2007).
- <sup>10</sup>G. Tian and Z. Xiao, "New insight on large-eddy simulation of flow past a circular cylinder at subcritical Reynolds number 3900," *AIP Adv.* **10**(8), 085321 (2020).
- <sup>11</sup>C. Ji, A. Munjiza, and J. J. R. Williams, "A novel iterative direct-forcing immersed boundary method and its finite volume applications," *J. Comput. Phys.* **231**(4), 1797–1821 (2012).
- <sup>12</sup>K. Kwon and H. Choi, "Control of laminar vortex shedding behind a circular cylinder using splitter plates," *Phys. Fluids* **8**(2), 479–486 (1996).
- <sup>13</sup>J. Kim and H. Choi, "Distributed forcing of flow over a circular cylinder," *Phys. Fluids* **17**(3), 033103 (2005).
- <sup>14</sup>G. Schewe, "On the force fluctuations acting on a circular cylinder in crossflow from subcritical up to transcritical Reynolds numbers," *J. Fluid Mech.* **133**, 265–285 (1983).
- <sup>15</sup>E. Achenbach and E. Heinecke, "On vortex shedding from smooth and rough cylinders in the range of Reynolds numbers  $6 \times 10^3$  to  $5 \times 10^6$ ," *J. Fluid Mech.* **109**, 239–251 (1981).
- <sup>16</sup>Y. Nakamura and Y. Tomonari, "The effects of surface roughness on the flow past circular cylinders at high Reynolds numbers," *J. Fluid Mech.* **123**, 363–378 (1982).
- <sup>17</sup>T. Igarashi, "Effect of tripping-wires on the flow around a circular cylinder normal to an airstream," *Jpn. Soc. Mech. Eng. Ser. B* **52**(473), 358–366 (1986) (translated).
- <sup>18</sup>F. S. Hover, H. Tvedt, and M. S. Triantafyllou, "Vortex-induced vibrations of a cylinder with tripping wires," *J. Fluid Mech.* **448**, 175–195 (2001).
- <sup>19</sup>A. Ekmecki and D. Rockwell, "Effects of a geometrical surface disturbance on flow past a circular cylinder: A large-scale spanwise wire," *J. Fluid Mech.* **665**, 120–157 (2010).
- <sup>20</sup>S. Bhattacharya and J. W. Gregory, "Investigation of the cylinder wake under spanwise periodic forcing with a segmented plasma actuator," *Phys. Fluids* **27**(1), 014102 (2015).
- <sup>21</sup>L. H. Feng, G. P. Cui, and L. Y. Liu, "Two-dimensionalization of a three-dimensional bluff body wake," *Phys. Fluids* **31**(1), 017104 (2019).
- <sup>22</sup>H. Park, R. Ajith Kumar, and M. M. Bernitsas, "Suppression of vortex-induced vibrations of rigid circular cylinder on springs by localized surface roughness at  $3 \times 10^4 \leq Re \leq 1.2 \times 10^5$ ," *Ocean Eng.* **111**, 218–233 (2016).
- <sup>23</sup>H. Zhu, Y. Gao, and T. Zhou, "Flow-induced vibration of a locally rough cylinder with two symmetrical strips attached on its surface: Effect of the location and shape of strips," *Appl. Ocean Res.* **72**, 122–140 (2018).
- <sup>24</sup>H. Sun, E. S. Kim, G. Nowakowski, E. Mauer, and M. M. Bernitsas, "Effect of mass-ratio, damping, and stiffness on optimal hydrokinetic energy conversion of a single, rough cylinder in flow induced motions," *Renewable Energy* **99**, 936–959 (2016).
- <sup>25</sup>J. H. Lee and M. M. Bernitsas, "Virtual damper–spring system for VIV experiments and hydrokinetic energy conversion," *Ocean Eng.* **38**, 732–747 (2011).
- <sup>26</sup>M. M. Bernitsas, "Harvesting energy by flow included motions," in *Springer Handbook of Ocean Engineering* (Springer International Publishing, Cham, 2016), pp. 1163–1244.
- <sup>27</sup>A. Vinod and A. Banerjee, "Surface protrusion based mechanisms of augmenting energy extraction from vibrating cylinders at Reynolds number  $3 \times 10^3$ – $3 \times 10^4$ ," *J. Renewable Sustainable Energy* **6**(6), 063106 (2014).
- <sup>28</sup>W. Xu, C. Ji, H. Sun, W. Ding, and M. M. Bernitsas, "Flow-induced vibration of two elastically mounted tandem cylinders in cross-flow at subcritical Reynolds numbers," *Ocean Eng.* **173**, 375–387 (2019).
- <sup>29</sup>W. Chen, C. Ji, J. Williams, D. Xu, L. Yang, and Y. Cui, "Vortex-induced vibrations of three tandem cylinders in laminar cross-flow: Vibration response and galloping mechanism," *J. Fluids Struct.* **78**, 215–238 (2018).
- <sup>30</sup>L. Ding, L. Zhang, M. M. Bernitsas, and C. C. Chang, "Numerical simulation and experimental validation for energy harvesting of single-cylinder VIVACE

- converter with passive turbulence control," *Renewable Energy* **85**, 1246–1259 (2016).
- <sup>31</sup>H. Zhu and Y. Gao, "Vortex induced vibration response and energy harvesting of a marine riser attached by a free-to-rotate impeller," *Energy* **134**, 532–544 (2017).
- <sup>32</sup>P. Han, G. Pan, and W. Tian, "Numerical simulation of flow-induced motion of three rigidly coupled cylinders in equilateral-triangle arrangement," *Phys. Fluids* **30**(12), 125107 (2018).
- <sup>33</sup>H. Zhu, H. Ping, R. Wang, Y. Bao, D. Zhou, X. Wei, and Z. Han, "Dynamic response of a cable with triangular cross section subject to uniform flow at Reynolds number 3900," *Phys. Fluids* **32**(4), 045103 (2020).
- <sup>34</sup>P. Parnaudeau, J. Carlier, D. Heitz, and E. Lamballais, "Experimental and numerical studies of the flow over a circular cylinder at Reynolds number 3900," *Phys. Fluids* **20**(8), 085101 (2008).
- <sup>35</sup>C. C. (Jim) Chang, R. Ajith Kumar, and M. M. Bernitsas, "VIV and galloping of single circular cylinder with surface roughness at  $3.0 \times 10^4 \leq Re \leq 1.2 \times 10^5$ ," *Ocean Eng.* **38**, 1713–1732 (2011).
- <sup>36</sup>Z. Shen, D. Wan, and P. M. Carrica, "Dynamic overset grids in OpenFOAM with application to KCS self-propulsion and maneuvering," *Ocean Eng.* **108**, 287–306 (2015).
- <sup>37</sup>X. Zhang, J. Wang, and D. Wan, "Numerical techniques for coupling hydrodynamic problems in ship and ocean engineering," *J. Hydrodyn.* **32**, 212–233 (2020).
- <sup>38</sup>Y. Zhuang and D. Wan, "Parametric study of a new HOS-CFD coupling method," *J. Hydrodyn.* **33**, 43–54 (2021).
- <sup>39</sup>W. Zhao, J. Wang, and D. Wan, "Vortex identification methods in marine hydrodynamics," *J. Hydrodyn.* **32**, 286–295 (2020).
- <sup>40</sup>J. Wang, W. Zhao, and D. Wan, "Development of naoe-FOAM-SJTU solver based on OpenFOAM for marine hydrodynamics," *J. Hydrodyn.* **31**(1), 1–20 (2019).
- <sup>41</sup>D. Deng, W. Zhao, and D. Wan, "Vortex-induced vibration prediction of a flexible cylinder by three-dimensional strip model," *Ocean Eng.* **205**, 107318 (2020).
- <sup>42</sup>X. Zhang, J. Wang, and D. Wan, "Euler-Lagrange study of bubble drag reduction in turbulent channel flow and boundary layer flow," *Phys. Fluids* **32**(2), 027101 (2020).
- <sup>43</sup>W. Zhao, L. Zou, D. Wan, and Z. Hu, "Numerical investigation of vortex-induced motions of a paired-column semi-submersible in currents," *Ocean Eng.* **164**, 272 (2018).
- <sup>44</sup>L. Ong and J. Wallace, "The velocity field of the turbulent very near wake of a circular cylinder," *Exp. Fluids* **20**(6), 441–453 (1996).
- <sup>45</sup>A. G. Kravchenko and P. Moin, "Numerical studies of flow over a circular cylinder at  $Re_D = 3900$ ," *Phys. Fluids* **12**(2), 403–417 (2000).
- <sup>46</sup>G. S. Cardell, "Flow past a circular cylinder with a permeable wake splitter plate," Ph.D. dissertation (California Institute of Technology, 1993).
- <sup>47</sup>T. Frederic, "Direct and large-eddy simulation of flow around a circular cylinder at subcritical Reynolds numbers," Ph.D. thesis (Fakultät für Maschinenwesen, 2002).
- <sup>48</sup>X. Ma, G. S. Karamanos, and G. E. Karniadakis, "Dynamics and low-dimensionality of a turbulent near wake," *J. Fluid Mech.* **410**, 29–65 (2000).
- <sup>49</sup>C. Norberg, "An experimental investigation of the flow around a circular cylinder: Influence of aspect ratio," *J. Fluid Mech.* **258**, 287–316 (1994).
- <sup>50</sup>E. Achenbach, "Distribution of local pressure and skin friction around a circular cylinder in cross-flow up to  $Re = 5 \times 10^6$ ," *J. Fluid Mech.* **34**(4), 625–639 (1968).
- <sup>51</sup>F. Bouak and J. Lemay, "Passive control of the aerodynamic forces acting on a circular cylinder," *Exp. Therm. Fluid Sci.* **16**(1–2), 112–121 (1998).
- <sup>52</sup>O. Posdziech and R. Grundmann, "Numerical simulation of the flow around an infinitely long circular cylinder in the transition regime," *Theor. Comput. Fluid Dyn.* **15**(2), 121–141 (2001).
- <sup>53</sup>K. Kamemoto, "Formation and interaction of two parallel vortex streets," *Bull. JSME* **19**(129), 283–290 (1976).
- <sup>54</sup>G. Chopra and S. Mittal, "Drag coefficient and formation length at the onset of vortex shedding," *Phys. Fluids* **31**(1), 013601 (2019).
- <sup>55</sup>C. Norberg, "Fluctuating lift on a circular cylinder: Review and new measurements," *J. Fluids Struct.* **17**(1), 57–96 (2003).
- <sup>56</sup>S. Dong, G. E. Karniadakis, A. Ekmekci, and D. Rockwell, "A combined direct numerical simulation–particle image velocimetry study of the turbulent near wake," *J. Fluid Mech.* **569**, 185 (2006).
- <sup>57</sup>H. Schlichting and K. Gersten, *Boundary-Layer Theory* (Springer Berlin Heidelberg, 2016).